

# Outcrop-scale fracture analysis and seismic modelling of a basin-bounding normal fault in platform carbonates, central Italy

T. Volatili<sup>a,\*</sup>, F. Agosta<sup>b,1</sup>, N. Cardozo<sup>c</sup>, M. Zambrano<sup>a,1</sup>, I. Lecomte<sup>d</sup>, E. Tondi<sup>a,e,1</sup>

<sup>a</sup> School of Science and Technology - Geology Division, University of Camerino, Italy

<sup>b</sup> Department of Sciences, University of Basilicata, Italy

<sup>c</sup> Department of Energy Resources, University of Stavanger, Norway

<sup>d</sup> Department of Earth Science, University of Bergen, Norway

<sup>e</sup> National Institute of Geophysics and Volcanology, Rome, Italy

## ARTICLE INFO

### Keywords:

Tight carbonates  
Fracture porosity  
Fracture permeability  
PSDM  
Seismic modelling

## ABSTRACT

Faults are characterized by a complex internal architecture. In carbonates, the geometry, attitude, and distribution of fault-related fractures and subsidiary faults can largely affect the petrophysical properties and hydraulic behavior of the fault zone. This work investigates the footwall damage zone of a seismic-scale normal fault (throw ~ 300 m) from a structural, petrophysical and seismic point of view. The studied Venere Fault (VF) bounds the intra-mountain Fucino Basin (central Italy) and crosscuts Lower Cretaceous platform carbonates. A significant portion of the footwall VF damage zone (VF-DZ) is well exposed in the 400 × 200 m Santilli Quarry. There, we assess the amount of outcrop-scale fracture porosity and permeability by in-situ fracture analyses and permeability measurements. The results show a composite power-law decay of fracture intensity away from the main slip surfaces, strongly influenced by subsidiary faults. An outcrop-based, digital 2D model of the VF-DZ is constructed and populated with acoustic properties (Vp, Vs and density) derived from both the matrix and fracture porosities. This model is enlarged five times and used for seismic modelling to investigate the seismic signature of the VF-DZ under different but realistic geological and geophysical conditions. Seismic modelling suggests that within the modelled damage zone and for wave frequencies of 20–40 Hz, seismic impedance contrasts associated with subsidiary faults may be imaged, depending on the degree of fracture porosity, fracture aperture, and the illumination angle (a measure of the maximum dip that can be imaged), the last two parameters being controlled by overburden depth. These results have implications for the seismic interpretation and characterization of fault zones in carbonates, and hence for the evaluation of fluid migration through these structures.

## 1. Introduction

The geometrical and structural properties of brittle faults are very difficult to characterize in the subsurface. Although seismic reflection data can be successfully used for fault network interpretation, a few studies document the architecture and seismic attributes of single faults (i.e., Cohen et al., 2006; Dutzer et al., 2010; Liao et al., 2019). Both seismic modelling and attribute-based interpretation have been employed to characterize the geometry of single fault zones, and assess their surrounding deformation (Botter et al., 2016; Alaei and Torabi, 2017; Cunningham et al., 2019) according to their seismic disturbance zone (Iacopini et al., 2016). In fact, although individual fractures are

usually below seismic resolution, their cumulative effect could be detected as a distortion of the seismic signal (Chopra and Marfurt, 2009; Li et al., 2015), and their main orientation estimated by structural seismic attributes (Michelena et al., 2013; Mendez et al., 2020). Synthetic fault models and their associated seismic response show the potential for characterizing damage zones using seismic attributes (Botter et al., 2017). However, since the interpretation in the subsurface of sub-seismic structures across fault zones (i.e., subsidiary faults, fracture networks) are often affected by either a limited spatial distribution of 1D well data or low-resolution of seismic data, it is not clear how the seismic anomalies from these areas correlate with actual fracture distribution and petrophysical properties.

\* Corresponding author.

E-mail address: [tiziano.volatili@unicam.it](mailto:tiziano.volatili@unicam.it) (T. Volatili).

<sup>1</sup> Reservoir Characterization Project ([www.rechproject.com](http://www.rechproject.com)).

<https://doi.org/10.1016/j.jsg.2022.104515>

Received 7 August 2021; Received in revised form 30 December 2021; Accepted 4 January 2022

Available online 10 January 2022

0191-8141/© 2022 The Authors.

Published by Elsevier Ltd.

This is an open access article under the CC BY-NC-ND license

(<http://creativecommons.org/licenses/by-nc-nd/4.0/>).

Fault damage zones, which commonly surround the fault cores, include thick volumes of fractured and faulted host rocks still preserving some of the original features such as bedding (Caine et al., 1996; Aydin, 2000; Gudmundsson et al., 2001; Sagy et al., 2001; Rotevatn et al., 2007). Within fault damage zones, many studies have documented common trends of both fracture density and intensity (Wilson et al., 2003; Faulkner et al., 2006, Mitchell and Faulkner, 2009; Savage and Brodsky, 2011; Johri et al., 2014; Ceccato et al., 2021). Although these trends have been verified in many outcrops, fracture parameters do not always scale proportionally with fault displacement (Anders and Wiltschko, 1994; Shipton and Cowie, 2003; Myers and Aydin, 2004; Mayolle et al., 2019; Mercuri et al., 2020). In this regard, several authors consider the role played by stress distribution along the evolving main slip surfaces on the localization of fault-related fracture clusters, assuming cohesive end zone models, different scales of mechanical unit thickness, and failure modes (Cowie and Scholz, 1992; Davatzes and Aydin, 2003; De Jossineau and Aydin, 2007a, 2007b; Camanni et al., 2021; Mayolle et al., 2021).

This work focuses on an integrated outcrop-based characterization and seismic modelling of a 100's m-thick footwall damage zone in low-porosity, platform carbonates. We investigate the complexity of the internal architecture of the fault zone from the structural, petrophysical, and seismic imaging points of view. The workflow is rooted on a field- and digital-based structural analysis. The studied fault, known as the Venere Fault (VF, Fig. 1), bounds eastward the intramontane Fucino Basin (Central Italy), and juxtaposes Lower Cretaceous platform carbonates on the footwall against Plio-Quaternary fluvio-lacustrine sediments on the hanging wall (Cavinato et al., 2002). By studying in detail the fractured and faulted carbonates exposed along the eastern and western walls of the active Santilli Quarry (Fig. 2), which are oriented

approximately orthogonal to the main slip surface (MSS), we assess the inner structure of the Venere fault damage zone (VF-DZ).

We document fracture distribution across the VF-DZ and show a fracture intensity decrease from the MSS following a composite power-law equation. The outcomes of fracture analyses are then used to estimate the contribution of fractures to porosity; in this regard, different scenarios of fracture aperture/length aspect ratio obtained from both field measurements and literature are considered (Olson, 2003; Schultz et al., 2008; Klimczak et al., 2010; Ghanbarian et al., 2019). Furthermore, in-situ permeability measurements are performed. As a result, a clear picture of petrophysical properties across the fault damage zone and poro-perm relations are obtained. Then, the resultant outcrop-scale 2D petrophysical model is further constrained by merging it with a virtual outcrop model of the fault zone, constructed using photogrammetry techniques. This base model has property zones (including acoustic properties) that obey the geometrical and spatial relationships observed in the outcrop. Finally, an enlarged version of the base model is used for seismic modelling and sensitivity analyses of both geological and geophysical parameters. Therefore, to evaluate the uncertainties in the seismic characterization and fluid-flow modelling of large faults in low-porosity carbonates, we integrate outcrop-based geological and petrophysical models of the VF-DZ with seismic modelling to generate seismic images of the fault zone.

## 2. Structural setting of the Fucino Basin

The Fucino Basin lies in the Peri-Adriatic outer portion of the central Apennines fold-and-thrust belt, Italy (Vezzani and Ghisetti, 1998; Vezzani et al., 2010). The central Apennines are characterized by primarily east-verging regional-scale thrusts, which formed during Late

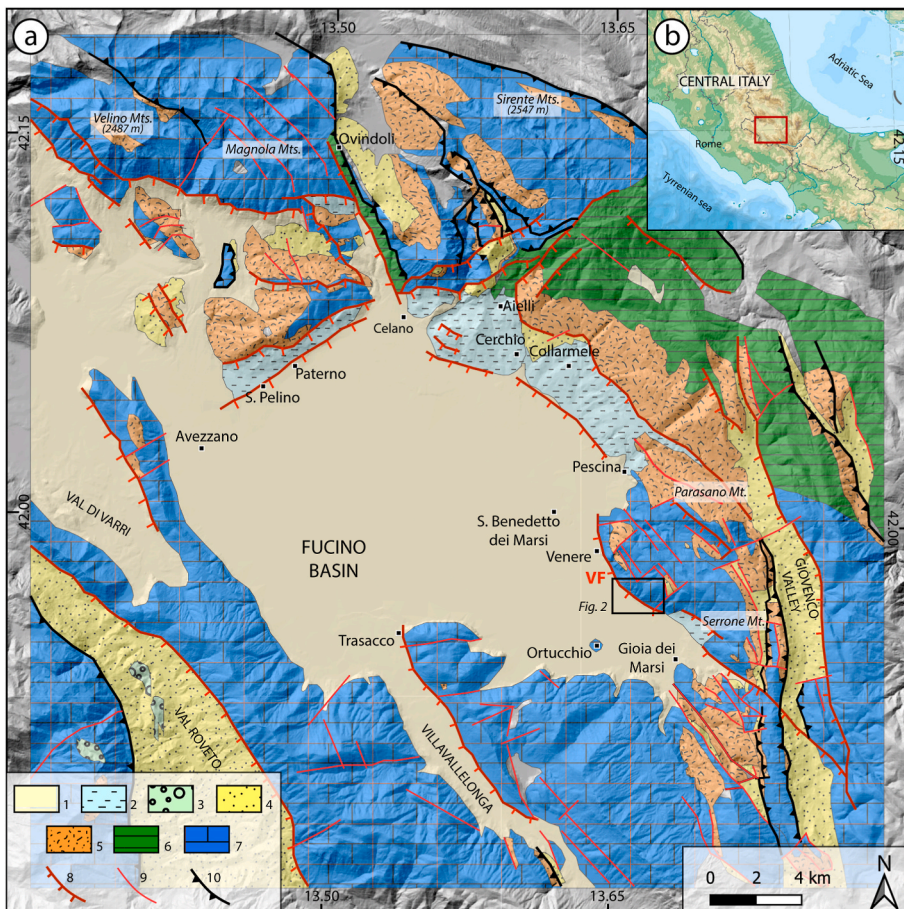


**Fig. 1.** (a) Geological map of the Fucino Basin and surrounding areas (modified after Cavinato et al., 2002). 1) Alluvial deposits (Upper Pleistocene–Holocene); 2) Lacustrine deposits (Upper Pleistocene–Holocene); 3) Lacustrine-lagoonal deposits (Upper Messinian); 4) Lazio–Abruzzi flysch deposits (Lower Messinian); 5) Marine carbonate ramp (Lower Miocene); 6) Slope and marginal Latium–Abruzzi carbonate platform (Eocene–Lower Cretaceous); 7) Inner carbonate platform (Upper Cretaceous–Middle Jurassic); 8) Normal fault; 9) Indistinct high-angle fault; 10) Thrust fault. (b) Inset showing the location of the Fucino Basin in central Italy.

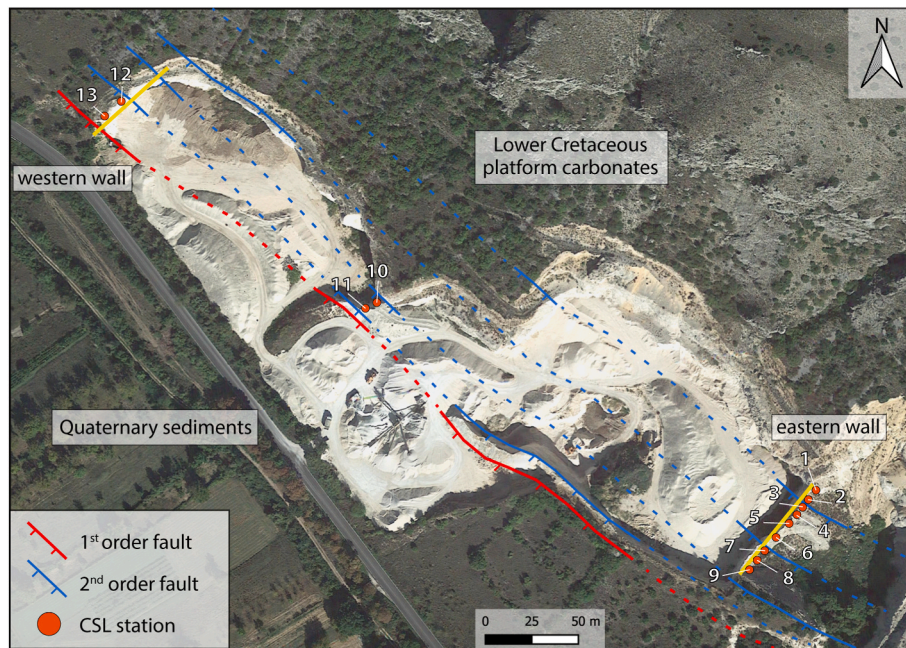


**Fig. 2.** Google Earth image (lat-long: 41.971°, 13.661°) of the study area with the main structural elements and studied sections. The 1st order fault is the main slip surface of the Venere Fault, and the study focuses on the northern footwall block, which consists of tight Lower Cretaceous platform carbonates. CSL stands for circular scanline.

Miocene–Pliocene compressional tectonics (Bigi et al., 1992; Ghisetti and Vezzani, 1999). Since Late Pliocene–Early Pleistocene, the imbricated fold-and-thrust belt has been crosscut and dissected by NW–SE striking normal faults, which mainly dip SW, and to a lesser degree by E–W striking normal faults. The central Apennines were uplifted and exhumed from shallow crustal depths during Plio–Quaternary times (Ghisetti and Vezzani 1999, 2002). As testified by the 1915 Avezzano earthquake ( $M_s = 7.0$ ), tectonic extension is still ongoing, with major seismic normal faults bounding the eastern side of the Fucino Basin (Boschi et al., 1997; Lanari et al., 2021 and references therein). Regarding the Avezzano earthquake, paleoseismological investigations document pure dip-slip extension (Michetti et al., 1996; Galadini and Galli, 1999), although minor right-lateral slip was determined in the Fucino Basin area by means of detailed fault scarps analysis (Piccardi et al., 1999). Overall, a ca. 300 m throw, and an average slip rate of 0.4–1.0 mm/year were estimated for the Venere fault and the study area of the Fucino Basin (Cavinato et al., 2002; Roberts and Michetti, 2004; Faure Walker et al., 2010).

In this work, we focus on key outcrops located within the active Santilli Quarry. There, the footwall damage zone of the Venere Fault (VF-DZ) is nicely exposed allowing a full 3D characterization (Fig. 2). The platform carbonates consist of Lower Cretaceous limestones (Vezzani and Ghisetti, 1998), which mainly include carbonate boundstones with very low values of porosity and permeability (Agosta et al., 2007). After detailed analysis of fracture attitude, nature, distribution, abutting and crosscutting relations, Agosta and Aydin (2006) identified the fundamental fracture modes and main structural elements related to the processes of VF-DZ nucleation and growth. These authors documented three different orders of subsidiary faults according to their dimension and throw. The 1st order fault includes the main slip surface (MSS) and a cataclastic fault core, up to 1 m-thick, made up of grain- and matrix-supported cataclasites (Agosta and Aydin, 2006; Ferraro et al., 2018; Merico et al., 2020). These fault rocks were partially cemented by meteoric-derived fluids, which mainly infiltrated along the MSS (Ghisetti et al., 2001; Agosta and Kirschner, 2003; Agosta, 2008). The 2nd order faults, sub-parallel to the main fault, are characterized by length on the order of few to several hundred meters and include cm-thick fault cores made up of grain-supported cataclasites and/or gouge. Due to

outcrop limitation the amount of displacement is not observable and was estimated on the order of several tens of meters according to their geometrical parameters (Agosta and Aydin, 2006). The 3rd order faults show throws on the order of several centimeters and their internal structure is mainly made up of brecciated carbonate rocks and rarely millimeters to centimeters thick cataclasites. Previous works along the VF-DZ also analyzed the mineralogical, petrographic, textural, petrophysical, and ultrasonic properties of the fault rock assemblage (Agosta et al., 2007; Ferraro et al., 2019, 2020). Based on petrophysical analyses, these authors documented a near linear porosity-permeability relationship in the uncemented fault rocks. On the contrary, the cemented cataclasites that localize along the MSS show constant low values of permeability, like the host rock permeability, and varying values of porosity. Ferraro et al. (2020) interpreted this behavior as due to the presence of moldic porosity associated with the selective dissolution of survivor grains within the cemented cataclasites.

### 3. Methods

We use a workflow designed to investigate the VF zone through an integrated multidisciplinary approach. The inner structure of the VF-DZ is analyzed by coupling structural data acquired in the field and digital-based measurements on virtual models of the outcrop. The petrophysical properties of the fault-related fracture network (fracture porosity and fracture permeability) are obtained by integrating in-situ permeability measurements with results of fracture analysis. The resulting VF-DZ model includes the variations of the estimated values of fracture porosity and acoustic properties (P-wave velocity, S-wave velocity, and bulk density). Finally, an enlarged version of this model is employed as input data to seismic modeling simulating different geological and geophysical scenarios, which provide useful information on the seismic character of the fault zone.

#### 3.1. Structural analysis

The field structural analysis was conducted along two exposed walls, respectively labelled as eastern and western, cropping out in the Santilli Quarry (Fig. 2). Both eastern and western walls, sub orthogonal to the

MSS, expose the VF footwall damage zone to its south-eastern tip and central portion, respectively.

3.1.1. Circular scan line analysis

A total of 13 circular scan line measurements (CSL) are performed at specific sites (orange circles in Fig. 2) to assess the amount of fracture properties across the VF-DZ. At each site, we calculate the values of fracture density ( $P_{20}$ ), which is the number of fractures per area [ $m^{-2}$ ], fracture intensity ( $P_{21}$ ), which is the sum of fracture length per area [ $m^{-1}$ ], and mean fracture length ( $l$ ), which is expressed in [ $m$ ]. In this work, we refer to fracture length as fracture traces on the studied

vertical walls. These parameters are estimated using the following equations (Mauldon et al., 2001):

$$P_{20} = \frac{m}{2\pi \times r^2} \tag{1}$$

$$P_{21} = \frac{n}{4r} \tag{2}$$

$$l = \frac{n}{m} \left( \frac{\pi r}{2} \right) \tag{3}$$

where  $n$  is the number of fracture intersections within a circular scan

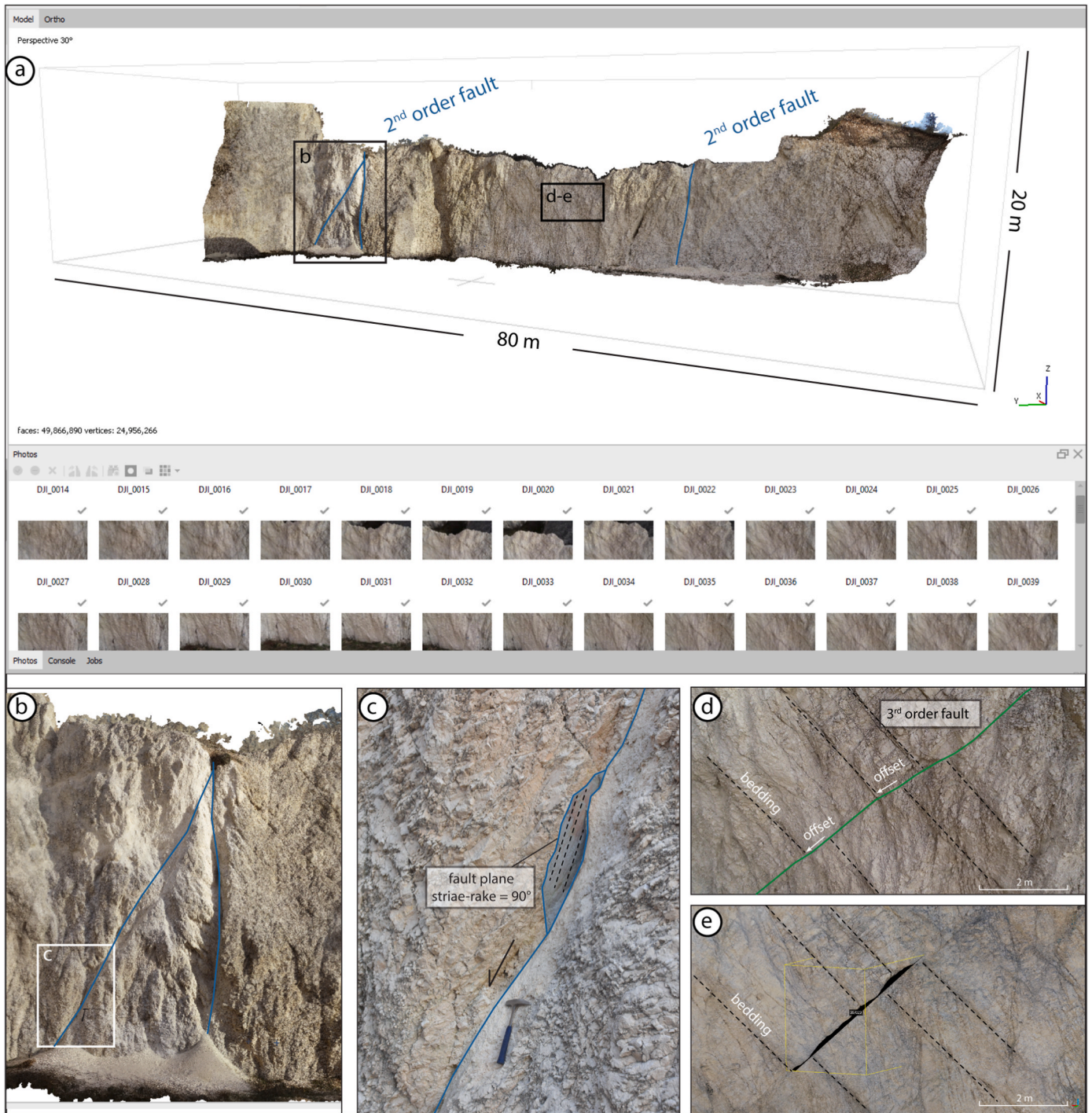


Fig. 3. (a) Virtual outcrop model of the eastern wall with interpreted 2nd order faults. (b) Close-up of a 2nd order fault and (c) field photo showing in detail the fault plane and striae (dashed lines). (d) Field photo showing a 3rd order fault and (e) dense point cloud of same area for measurements.

line, and  $m$  is the number of fracture terminations within the circular scan line. An optimal circle radius  $r$  of 0.1 m was chosen to avoid biases related to undersampling of fractures (Rohrbaugh et al., 2002), and multiple heterogeneity domains in a single survey. The required minimum number of 30 fracture terminations is always respected. Thus, the CSL size and the derived fracture properties (porosity and permeability) are assumed to be representative of single sampling stations.

CSL analyses document the variation of both fracture density and intensity as a function of distance to both the main fault and the subsidiary faults, which respectively correspond to the 1st and 2nd order faults of Agosta and Aydin (2006). In small and isolated faults, the fracture density decreases away from the fault generally following a power law function (Savage and Brodsky, 2011). However, in more complex and large faults, the fracture density is generally characterized by more irregular distributions due to the presence of subsidiary faults and their related localized deformation. Savage and Brodsky (2011) proposed modelling the composite curve of fracture intensity across a fault zone characterized by subsidiary faults using a superposition of power-law functions. Following the same approach, we decomposed the estimated fracture intensity distribution into two main power-law functions, which correspond to the main and subsidiary faults, respectively. To obtain the coefficients of both power-law equations, an optimization approach was adopted by using a generalized reduced gradient nonlinear algorithm (Lasdon et al., 1974). This procedure consists of iteratively varying the constants of the power-law equations until the lowest sum of squared errors between the best-fit model and the data is obtained. Since the 3rd order faults are characterized by poorly developed, vertically discontinuous damage zones (Agosta and Aydin, 2006), their contribution is not incorporated in the fracture intensity decay model.

### 3.1.2. Photogrammetry analysis

Photogrammetric surveys were performed along both eastern and western walls by means of an Unmanned Aerial Vehicle (UAV). Then, by using the Structure from Motion (SfM) technique, we construct a virtual outcrop model (James and Robson, 2012). The aerial photographs were taken using the DJI Phantom 4 Pro UAV, which is equipped with a 20Mp onboard camera, and 1 inch image sensor. In the field, the UAV flew at distances between ~2 and 5 m from the studied walls. Each digital model was then built using ~200 overlapping photos. The general SfM processing procedure follows the methods described by Pitts et al. (2017) using the Agisoft Metashape software (Fig. 3a). The output from the virtual outcrops consist of high-resolution surface meshes containing more than 30 million faces, and associated point clouds (up to 250 million points).

The main advantage of using virtual outcrop models is the ability to obtain additional information regarding the geometry of subsidiary structural elements in the footwall VF-DZ (Fig. 3 b-e). The point clouds were imported into the CloudCompare software for further interpretation, and to measure length, throw, dip direction and dip angle of subsidiary 2nd order faults (Fig. 3e). These data were obtained by using a semi-automatic fracture tracing method (Thiele et al., 2017). In addition, the high resolution orthomosaics (near 1.5 mm/pix) from the virtual outcrop model were used for the construction of the VF-DZ base model. The eastern and western walls orthomosaics were merged into a single 2D section representing the footwall DZ. In this model, the 2nd order faults and the largest 3rd order faults cover a more representative area. Subsequently, the entire 2D geological model is populated with petrophysical and acoustic properties, as described in the following section.

## 3.2. Petrophysical and acoustic properties

### 3.2.1. Fracture porosity

The amount of fracture porosity was calculated from the fracture density ( $P_{20}$ ) across the damage zone, using the following equation:

$$\varphi_{CSL} = P_{20} \times l \times E \quad (4)$$

where  $l$  is the mean fracture length calculated from the CSL analysis, and  $E$  is the mechanical fracture aperture estimated from a linear relationship with the fracture length. Many studies focusing on fracture scaling relations, involving multiple fracture datasets, have demonstrated that the trend of this linear relationship (aperture/length) varies between 0.01 and 0.001 (e.g., Olson, 2003; Schultz et al., 2008; Klimczak et al., 2010; Ghanbarian et al., 2019, and reference therein). This linear fracture aperture/length relationship was further validated from field measurements (cf. Ch. 4.1). In this regard, we evaluated three scenarios of fracture porosity by varying the ratio  $E/l$ :

- i.  $\Phi_{CSL1}$ , which assumes  $E/l = 0.01$  and returns an average fracture aperture likely related to a relatively low confining pressure condition;
- ii.  $\Phi_{CSL2}$ , which assumes  $E/l = 0.005$  and represents the trend of fracture aperture/length measured in the studied outcrop;
- iii.  $\Phi_{CSL3}$ , which assumes  $E/l = 0.001$  and results in very small average fracture aperture values, likely resembling the fracture aperture at greater, kilometer depths.

### 3.2.2. Fracture permeability

In-situ permeability measurements were carried out using a portable air permeameter, TinyPerm (Balsamo et al., 2010; Filomena et al., 2014; Tondi et al., 2016). To avoid biases due to surface irregularities and weathering, the sampling sites were cleaned and cleared out of detritus (Antonellini et al., 2014; Riegel et al., 2019). A maximum of 9 measurements were taken at each CSL station.

To obtain a reliable permeability value at each CSL station and avoid the use of fracture roughness correction factors (Zambrano et al., 2019 and reference therein), the hydraulic aperture,  $e$ , is first calculated using the equation for smooth parallel plates (Snow, 1969):

$$e = \sqrt{k_i \times 12} \quad (5)$$

where  $k_i$  [ $\text{m}^2$ ] is the average permeability for each CSL station, derived from the permeability measurements. Then, the fracture permeability  $k_f$  is calculated as follows:

$$k_f = \frac{n}{L} \left( \frac{e^3}{12} \right) \quad (6)$$

where  $n/L$  is the linear fracture intensity [ $\text{m}^{-1}$ ], the number of fractures ( $n$ ) per unit of length ( $L$ ). To take advantage of our areal fracture survey approach, eq. (6) was modified to obtain the equivalent fracture permeability  $k_e$  as follows:

$$k_e = P_{21} \left( \frac{e^3}{12} \right) \quad (7)$$

The impact of fracture orientation was not considered for the estimation of the equivalent fracture permeability. However,  $k_e$  was assumed to resemble the along-fault permeability component since the in-situ permeability measurements were taken in single fractures oriented sub-parallel to the MSS. According to the CSL analyses, the fractures are highly connected and therefore we assume that the fracture network is above the percolation threshold.

### 3.2.3. Seismic velocities and density

To perform the seismic modelling of the VF-DZ, the base model was populated with the P wave velocity  $V_p$ , S wave velocity  $V_s$ , and density, estimated from the field measurements. The  $V_p$  was derived from the porosity estimates by discriminating the effect of fracture and matrix porosity according to Kumar and Han (2005). These authors use a differential effective medium (DEM), which defines the contribution of interparticle pores (matrix) and crack-shaped pores (fractures) on

P-wave velocity. To automate the selection of Vp values, we used a Matlab function powered by the curve fitting toolbox, which includes both matrix and fracture porosity components and delivers a Vp value in agreement with Kumar and Han (2005). For the sake of simplification of the implemented Vp-porosity relationship, the effect of fracture and matrix pore network anisotropy was not considered. For matrix porosity, we considered values ~0.8% as reported by Agosta et al. (2007). For the fracture porosity, we used the values estimated in section 3.2.1. The Vs values were obtained using a Vp/Vs ratio of 1.9, which is typical for carbonates (Miller, 1992). The seismic velocities and density of the fault core were assigned using data from Agosta et al. (2007). Finally, the bulk density,  $\rho$ , was calculated assuming a water saturated porous medium, using the following equation:

$$\rho = \rho_m(1 - \Phi) + \rho_f\Phi \tag{9}$$

where  $\rho_m$  is the matrix density, which is equivalent to the density of calcite (2.71 g/cm<sup>3</sup>),  $\rho_f$  is the density of the fluid (water, 1.0 g/cm<sup>3</sup>), and  $\Phi$  is the total porosity, including both fracture and matrix porosity.

### 3.3. Seismic modelling

Seismic imaging simulations were used to evaluate the seismic expression of the VF-DZ and the inner structures considering different geological and geophysical scenarios. A based grid was built by combining information from the virtual outcrops and petrophysical and acoustic properties. Data obtained from the eastern and western walls

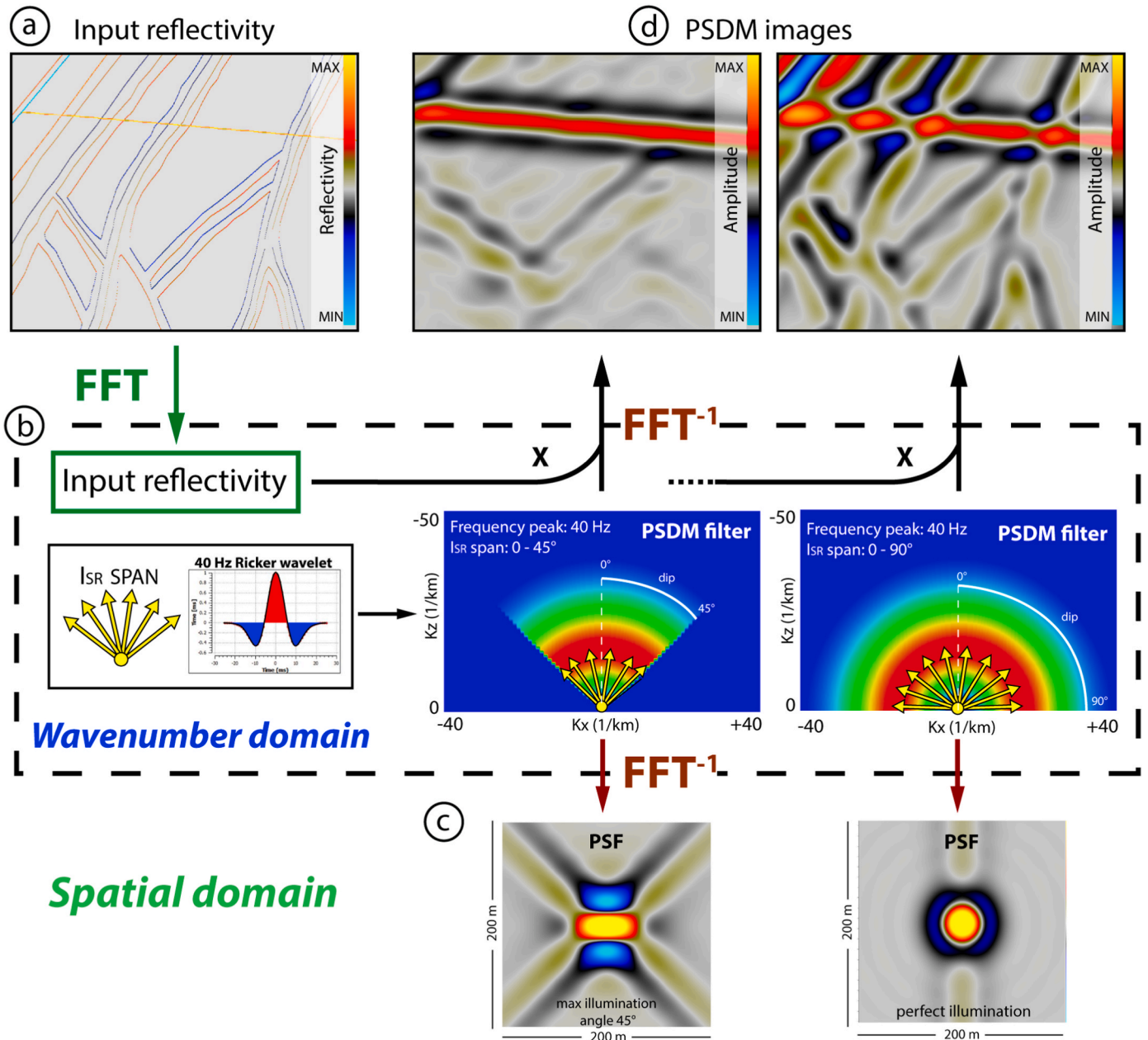


**Fig. 4.** Workflow and basic elements for generating PSDM seismic images. (a) 2D input reflectivity model, which is converted to the wavenumber domain through a Fast Fourier Transform (FFT). (b) The PSDM filters are generated in the wavenumber domain by combining a selected dominant frequency Ricker wavelet with an assigned maximum illumination angle ( $I_{SR}$  span; Lecomte, 2008), here varying from 45° to 90° (perfect illumination). (c) The PSFs are obtained in the spatial domain by inverse Fast Fourier Transform ( $FFT^{-1}$ ) of PSDM filters. (d) Finally, the PSDM images are generated by the product of the input reflectivity grid with the PSDM filters in the wavenumber domain and converted to the spatial domain by applying an inverse Fast Fourier Transform ( $FFT^{-1}$ ).

were merged into a single 2D section representing the footwall VF-DZ (Fig. 11). The fracture domains (FDs) were extrapolated to a larger scale to include the surrounding geology of both the footwall and the hanging wall. This resulted in a more complete fault zone model, which is less biased by low contrasts of seismic impedance.

The synthetic seismic data were generated using the pre-stack depth migration (PSDM) simulator implemented in the SeisRoX™ software. This simulator reproduces the effects of seismic imaging on the PSDM domain by acting as an image-processing method distorting an input reflectivity grid (Lecomte, 2008; Lecomte et al., 2015; Lecomte and Kaschwich, 2018). PSDM images can thus be rapidly simulated by spatial convolution with detailed 3D reflectivity models. This methodology was previously successfully employed to reproduce synthetic seismic images of faults and folds (Botter et al., 2014, 2016; Wood et al., 2015; Anell et al., 2016; Lecomte et al., 2016; Grippa et al., 2019; Wrona et al., 2020).

This method considers a spatial convolution operator called the Point-Spread Function (PSF), which ideally depends on the acquisition geometry, velocity model, and input wavelet, involving 3D angle-dependent illumination and resolution effects (Lecomte, 2008; Lecomte et al., 2015, 2016). The workflow and basic elements included in the 2D PSF-based convolution approach are shown in Fig. 4, whereas an extended description of this technique is given in Lecomte (2008). The main input to the PSDM simulator is an incident angle-dependent reflectivity model (Fig. 4a), which is derived from the acoustic properties of the model, i.e., density,  $V_p$  and  $V_s$ . In the absence of a given survey and background velocity model, as is the case for the present work, an angle of maximum illumination and a selected incident angle suffice to form a generic PSDM filter, which can be combined with a wavelet to add the frequency dependency (Fig. 4b). The angle of maximum illumination means that geological dips steeper than that angle will not be imaged. In the spatial domain, the PSF is the Fourier-equivalent of the PSDM filter in the wavenumber domain obtained by applying an inverse Fast Fourier transform ( $FFT^{-1}$ ) to the PSDM filter (Fig. 4c). The modelling can thus also be seen as a convolution in the spatial domain between the input reflectivity and the PSF. In the wavenumber domain, the PSDM filters are multiplied with the reflectivity grid after first converting the latter by Fast Fourier transform (FFT), and an inverse FFT ( $FFT^{-1}$ ) of the product yields the final

simulated PSDM image (Fig. 4d).

### 3.3.1. Geological and geophysical parameters

For the simulations, we focus on understanding the seismic expression of the fault damage zone under different geological and geophysical parameters as summarized in Fig. 5. Most of the VF-DZ structures are at sub-seismic scales and would not be detected in industry seismic at km depths (~20–40 Hz frequencies). To test the impact of a structure like the VF-DZ at such depths and with standard seismic frequencies, we enlarged five times the geological model. This procedure is reasonable since fault zones mostly have a fractal nature, which means that their dimension scales with fault displacement (Fossen and Gabrielsen, 1996; Faulkner et al., 2011; Torabi et al., 2020), whereas their fracture abundance variation is insensible to fault size (Scholz, 2019, and references therein). Scibek (2020) also highlights the occurrence of similar petrophysical properties in fault damage zones regardless of their dimension.

Since the field data are limited to the footwall of the VF-DZ, we build three different geological models (GMs), which differ in terms of surrounding lithology above (footwall) and adjacent (hanging wall) to the outcrop model as follows:

- i. GM1 carbonates with 10% matrix porosity.
- ii. GM2 carbonates with 5% matrix porosity.
- iii. GM3 saturated flysch with constant acoustic properties:  $V_p = 2.5$  km/s,  $V_s = 0.8$  km/s, and density =  $2.2 \text{ g/cm}^3$  (data from Patruno and Scisciani, 2021; Mancinelli et al., 2021).

These three models test the effect of different surrounding impedance contrasts on the seismic signature of the VF-DZ. In the GM1 and GM2 models, the VF-DZ is surrounded by the lithology observed in the footwall. In the GM3 model, however, the fault zone is surrounded by flysch of the Fucino Basin. For the three models, the petrophysical and acoustic properties of the carbonates are varied by considering three fracture aperture scenarios corresponding to 0.01, 0.005, and 0.001 times the mean fracture length of the fault zone as stated in section 3.2.1 (Fig. 5). To test the effect of these different geological parameters, the geophysical parameters are fixed, and they include a Ricker wavelet of 30 Hz dominant frequency, and a 60° illumination angle. To complete

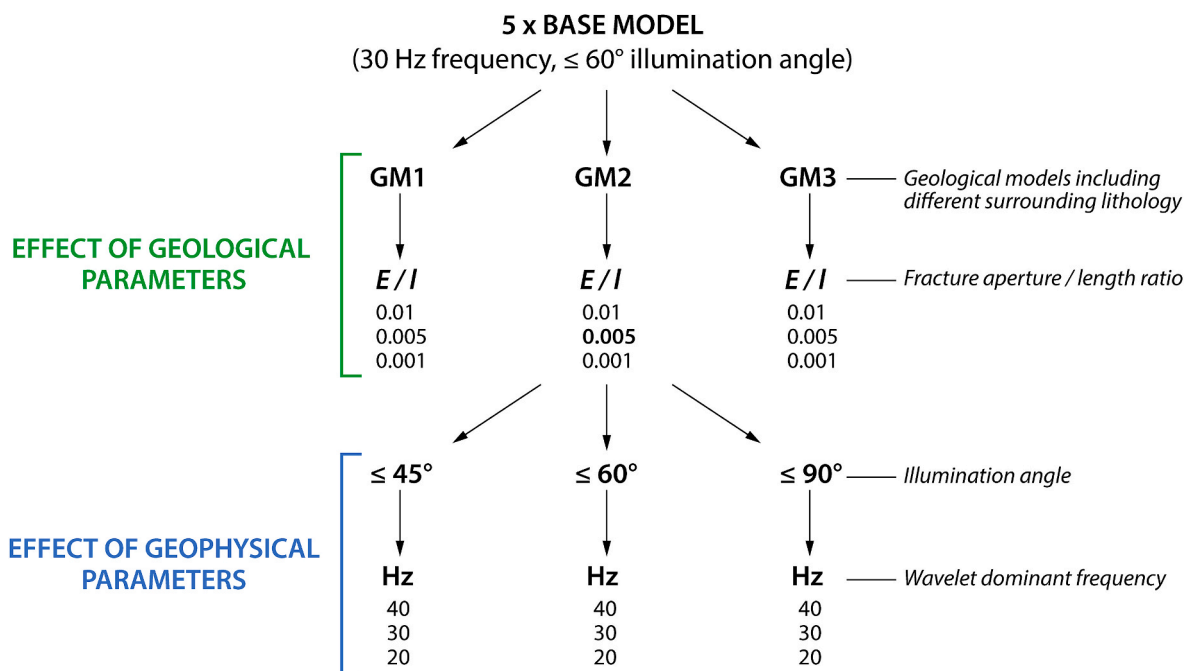


Fig. 5. Chart flow of the seismic models indicating both the geological and geophysical parameters that were tested.

the sensitivity analysis, geophysical parameters controlling the PSF are varied for the model GM2. Specifically, we test the effect of different illumination angles (45, 60 and 90°), and wavelet frequencies (20, 30 and 40Hz).

#### 4. Results

##### 4.1. Fracture properties

The VF-MSS (1st order fault) is laterally continuous throughout the study area (Fig. 2). The strike of this fault varies from S42E (southern edge of the Santilli Quarry) to S64E (northern edge), whereas its dip angle is ≈ 50° SW. The well-developed slickenlines present on the fault planes show pitch angles forming clusters at ca. 90° and ca. 105° along the southern and northern edges of the quarry, respectively. The 100 m-thick footwall VF-DZ includes four 2nd order faults, which roughly strike NW-SE, and form high-angle synthetic structural elements with respect to the MSS (Figs. 2 and 3). The spacing between adjacent 2nd order faults increases away from the MSS. Hereafter, we document the detailed architecture of two walls orthogonal to the MSS labelled as

eastern and western walls, respectively.

The eastern wall is crosscut by two 2nd order faults (Figs. 2 and 6a). The 2nd order fault closer to the MSS strikes S55E, and dips 65° SW, whereas the other one strikes S46E, and dip 85° SW. The latter fault is associated with a conjugate splay oriented S54E/64° NE. The amount of displacement solved by these faults cannot be established. Both 2nd order faults include a few m-thick fault damage zones encompassing uncemented (poorly cemented in places) fault cores made up of 5–20 cm-thick cataclasites (Fig. 7a and b). We document a total of 47 3rd order faults. Overall, they strike N80W to N30W, dip 50–80° NE (Fig. 6c), and are hence antithetic to the MSS. Based upon the offset of the carbonate beds, the 3rd order faults are characterized by throw values ranging from 5 to 60 cm. These faults are made up of discontinuous pods of brecciated carbonates that localize along the slip surfaces (Fig. 7c). We note that the bedding attitude along the whole eastern wall varies from ca. S60E/45° SW, away from the MSS, to ca. S60E/60° SW close to it.

The western wall exposes the MSS, and it is crosscut by two 2nd order faults striking ≈ S50E, and dipping 60° to 70° SW (Fig. 6b). These 2nd order faults are therefore synthetic to the MSS. The amount of

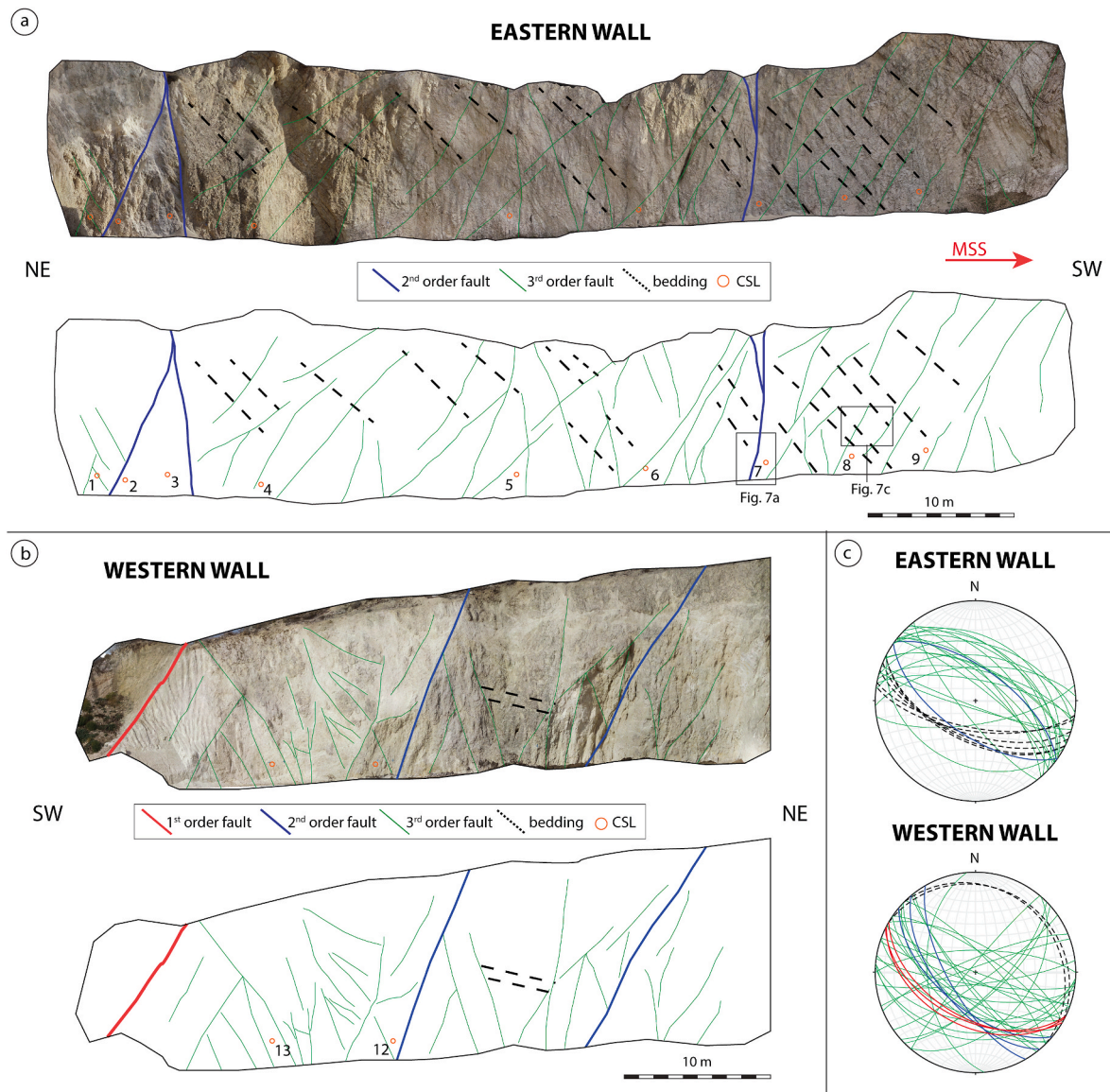
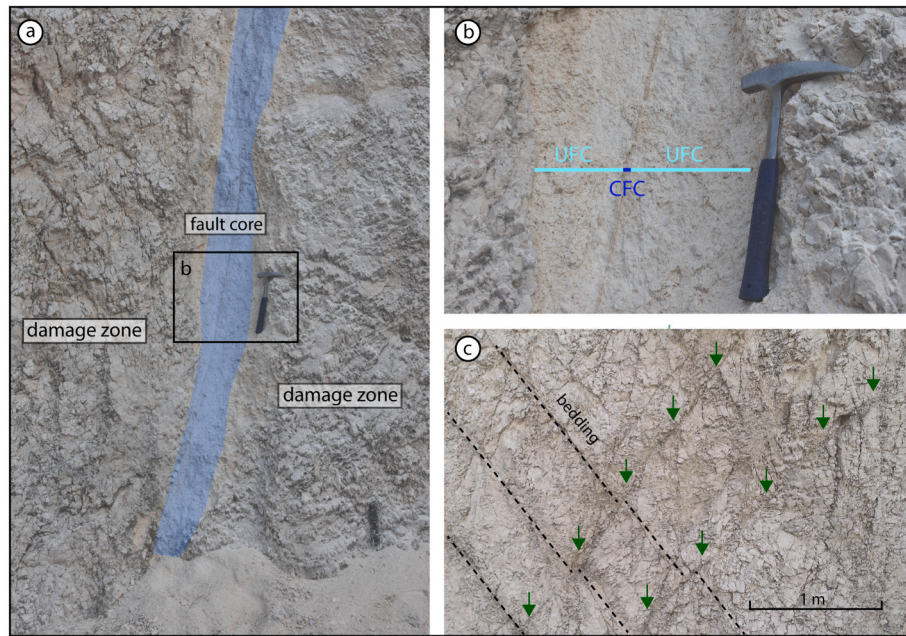


Fig. 6. Orthomosaics and line drawings of the structures observed along the a) eastern wall and b) western wall. c) Faults and bedding planes in lower hemisphere, equal area stereonets. Lines' legend is similar to (a) and (b). CSL# show the location of the circular scan lines.



**Fig. 7.** Detail of the inner architecture of subsidiary faults on the eastern wall. a) 2nd order fault zone and associated close-up in (b), b) un cemented (UFC) and cemented (CFC) fault rocks, c) two 3rd order faults highlighted by green arrows, including pods of fault breccia and clearly offsetting bedding. (For interpretation of the references to colour in this figure legend, the reader is referred to the Web version of this article.)

displacement solved by these faults cannot be established. Their inner structure is made up of 5–10 cm-thick cataclasites. The western wall is also crosscut by 39 3rd order faults, most of which are synthetic to the MSS fault. Altogether, these subsidiary faults show a wider range of attitudes with respect to those crosscutting the eastern wall. They strike S40W to S20E, and dip 40–80° W (Fig. 6c). Regarding the amount of displacement, it is not possible to establish it due to the lack of evident stratigraphic markers. The inner structure of these faults includes 2 to 5 cm-thick un cemented fault core, mainly characterized by fragmented and comminuted carbonates. We note that the density of the 3rd order faults is not homogeneous within the western wall, showing an increment by a factor of ca. 2 approaching the MSS (from about 20 m-distance). The bedding attitude measured along the western wall is somehow constant at values of ca. N30W/15° NE.

The results of the CSL analyses are summarized in Table 1, and reported in Fig. 8a and 8b. The computed values of fracture density ( $P_{20}$ ), fracture intensity ( $P_{21}$ ), and mean fracture length ( $l$ ) are also shown as normalized values with respect to the largest ones (Fig. 8b). Linear fracture aperture/length relations are documented for the two study outcrops of the footwall VF-DZ (Fig. 8c).

Although it is difficult to distinguish in the field the extent of 2nd order fault damage zones from surrounding deformation, a further analysis of the fracture intensity ( $P_{21}$ ) shows that it decreases as function of distance ( $D$ ) from the MSS and that it can be decomposed into two main trends, which are related to the 1st and 2nd order faults (Fig. 9). The optimal solution obtained by applying the minimum squares technique generates a modelled decay with a mean absolute error (MAE) of 0.07 (dashed black line in Fig. 9). The modelled decay of fracture intensity is represented by power-law functions ( $P_{21} = c \times d^{-n}$ ), as reported in the literature (Savage and Brodsky, 2011). It consists of a main, broader decay with an exponent  $n = 0.5$ , a scaling factor  $c = 700$ , and a distance  $D$  (dashed red line in Fig. 9), representative of the 1st order fault; and smaller, more localized decays with  $n = 0.52$ ,  $c = 56$ , and distance to the subsidiary structure  $d_i$ , representative of the 2nd order faults.

**Table 1**

Data derived for the single CSL stations.  $P_{20}$  = fracture density;  $P_{21}$  = fracture intensity;  $l$  = mean fracture length;  $\Phi_{CSL1}$ ,  $\Phi_{CSL2}$  and  $\Phi_{CSL3}$  = fracture porosities from CSL analysis with  $E/l = 0.01$ , 0.005 and 0.001, respectively;  $k_e$  = median value of fracture equivalent permeability (Eq. (7)).

| CSL_ID | $P_{20}$<br>[m <sup>-2</sup> ] | $P_{21}$<br>[m <sup>-1</sup> ] | $l$<br>[cm] | $\Phi_{CSL1}$<br>[%] | $\Phi_{CSL2}$<br>[%] | $\Phi_{CSL3}$<br>[%] | $k_e$<br>[m <sup>2</sup> ] |
|--------|--------------------------------|--------------------------------|-------------|----------------------|----------------------|----------------------|----------------------------|
| 1      | 5.4E+03                        | 112.5                          | 2.0         | 2.24                 | 1.12                 | 0.22                 | 5.83E-15                   |
| 2      | 7.3E+03                        | 170                            | 2.3         | 3.57                 | 1.78                 | 0.36                 | 3.18E-13                   |
| 3      | 5.6E+03                        | 132.5                          | 2.4         | 2.80                 | 1.40                 | 0.28                 | 7.71E-14                   |
| 4      | 5.0E+03                        | 115                            | 2.4         | 2.44                 | 1.22                 | 0.24                 | 5.41E-13                   |
| 5      | 8.5E+03                        | 137.5                          | 1.6         | 2.56                 | 1.28                 | 0.26                 | 1.65E-14                   |
| 6      | 5.8E+03                        | 132.5                          | 2.3         | 2.73                 | 1.37                 | 0.27                 | 9.17E-13                   |
| 7      | 9.0E+03                        | 187.5                          | 2.1         | 3.79                 | 1.90                 | 0.38                 | 1.89E-14                   |
| 8      | 5.8E+03                        | 135                            | 2.3         | 2.77                 | 1.38                 | 0.28                 | 7.53E-14                   |
| 9      | 6.6E+03                        | 117.5                          | 1.8         | 2.34                 | 1.17                 | 0.23                 | 2.85E-13                   |
| 10     | 9.3E+03                        | 172.5                          | 1.9         | 3.38                 | 1.69                 | 0.34                 | 1.59E-12                   |
| 11     | 9.6E+03                        | 190                            | 2.0         | 3.93                 | 1.97                 | 0.39                 | 1.75E-12                   |
| 12     | 8.9E+03                        | 185                            | 2.1         | 3.89                 | 1.94                 | 0.39                 | 2.3E-15                    |
| 13     | 1.9E+04                        | 265                            | 1.6         | 4.85                 | 2.43                 | 0.49                 | 1.11E-12                   |

#### 4.2. Petrophysical properties

The calculated fracture porosity ( $\Phi_{CSL}$ ) and the equivalent fracture permeability ( $k_e$ ) are summarized in Table 1 and Fig. 10. In general, across the VF-DZ both fracture porosity and permeability show a decreasing trend away from the MSS, which is consistent with the reported fracture intensity decay. The fracture permeability derived from

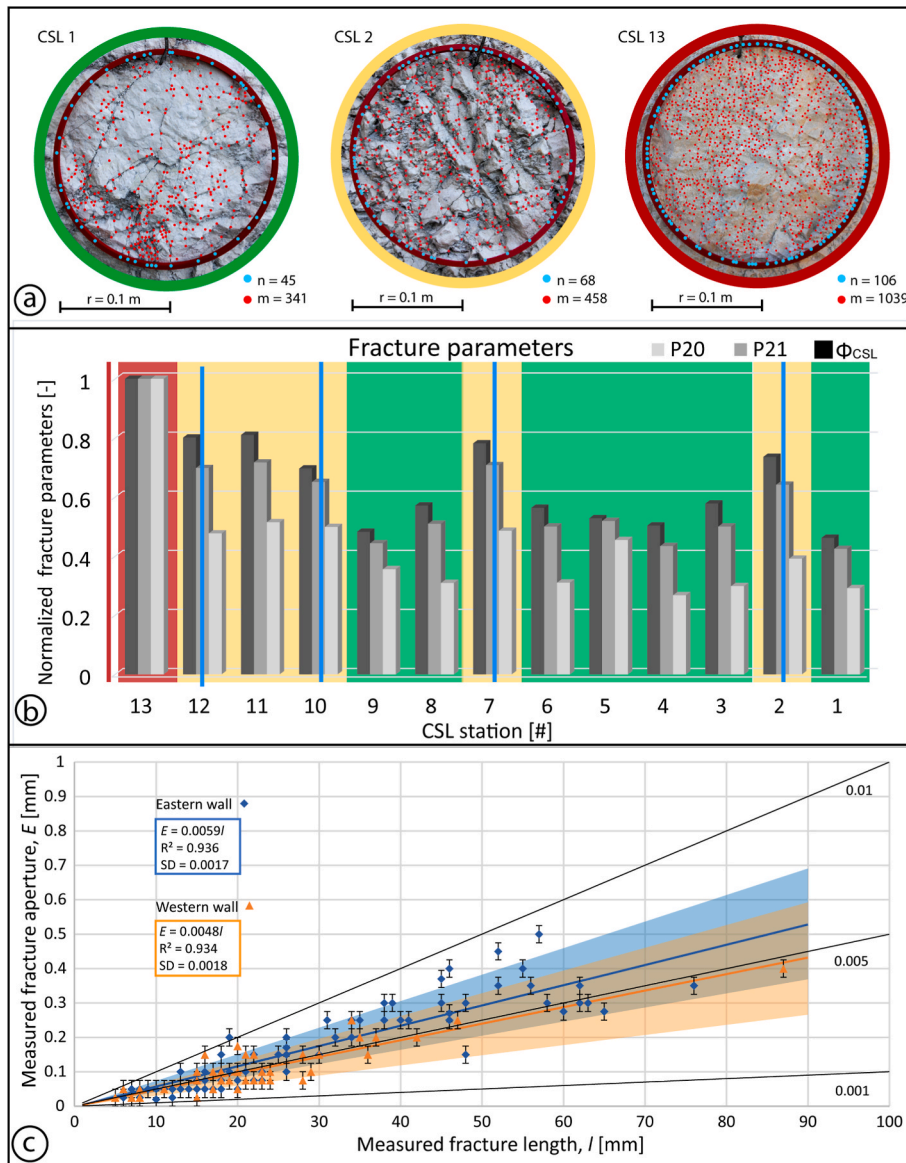


**Fig. 8.** (a) Examples of circular scan lines CSL (circle radius = 0.1 m) from the eastern wall (1 and 2), and western wall (13). Blue dots (n) are fracture intersections, and red dots (m) are fracture terminations. (b) Normalized  $P_{20}$ ,  $P_{21}$ , and  $\Phi_{CSL}$  histograms. The red and blue lines show the position of the 1st and 2nd order faults, respectively. Colors in the background refer to the fracture domains: fragmented (red), highly fractured (yellow) and moderately fractured (green) carbonates. (c) Plot of the fracture mechanical aperture,  $E$ , and length,  $l$ , measured at the eastern (blue diamonds) and western (orange triangles) walls. Error bars ( $\pm 0.025$  mm) were assigned to the mechanical aperture due to limitation of sampling resolution. The regression lines are surrounded by halos representing the standard deviation, SD. The black lines refer to the fracture aspect ratio  $E/l$  used for the models presented in this study. (For interpretation of the references to colour in this figure legend, the reader is referred to the Web version of this article.)

field CSL measurements shows median values ranging from  $1.1 \times 10^{-12}$  to  $5.8 \times 10^{-15} \text{ m}^2$ . The range of variability at each CSL station is between 1 and 2 orders of magnitude, for the first and third quartile values of the permeability distribution, respectively (Fig. 10). Generally, the calculated values of permeability are in agreement with the values of fracture porosity documented for the fracture domains. However, close to the 2nd order faults (CSL #2, #7, #12), the calculated values of fracture permeability are 3 orders of magnitude lower than the surrounding rock, regardless of the estimated high fracture porosity values (Fig. 10).

The  $\Phi_{CSL}$  values [%] are strongly dependent on the adopted fracture aspect ratio ( $E/l$ ). The high-end member ( $\Phi_{CSL1}$ ),  $E/l = 0.01$ , gives an average mechanical aperture,  $E$ , of 0.2 mm with  $\Phi_{CSL}$  values ranging from 2.2 to 4.9%. On the other hand, the low-end member ( $\Phi_{CSL3}$ ),  $E/l = 0.001$ , gives an average mechanical aperture,  $E$ , of 0.02 mm with  $\Phi_{CSL}$  values not exceeding 1%. The combined analysis of fracture density/intensity and fracture porosity is therefore key to assess the three main fracture domains (FD, Fig. 8b). We also compare the values obtained for these domains with those after the most conservative case,  $E/l = 0.005$ , which is the most representative scenario for the studied outcrop, in light of the measured fracture aperture/length trends (Fig. 8c). The first fracture domain ( $\Phi_f > 2.1\%$ ) corresponds to fragmented carbonates,

which are present close to the MSS (<20 m from the MSS, western wall of the quarry). The second domain is highly fractured ( $\Phi_f = 1.6\text{--}2.20\%$ ), and corresponds to rock volumes located 20–40 m away from the MSS. The third domain is moderately fractured ( $\Phi_f = 1.1\text{--}1.6\%$ ) and is present >40 m away from the MSS and 5-to-20 m away from the 2nd order faults. This domain includes all meso-scale fault-related fractures and those associated with the 3rd order faults (Fig. 8b). Within the most deformed zones (i.e., in proximity of the MSS or 2nd order faults), the fracture network is characterized by a higher fracture intensity but a smaller fracture dimension (i.e., length and aperture). Furthermore, the fracture aspect ratio in these areas can be smaller than in the less deformed carbonate rocks, as demonstrated by the lower fracture aperture-length trend of the western wall with respect to the eastern wall (Fig. 8c).

#### 4.3. Petrophysical and seismic velocity model

Since the amount of fracture porosity is modelled as a function of distance from 1st and 2nd order faults (Fig. 11), we include the three FDs (fragmented, highly fractured, and moderately fractured carbonates) in the 2D base model. In addition, far ( $\approx 130$  m) from the MSS, the

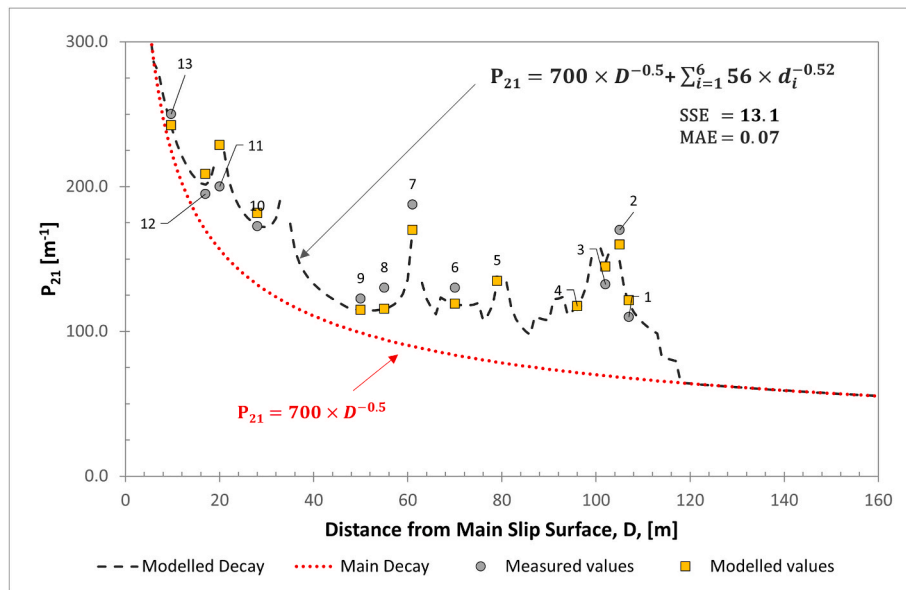


Fig. 9. Decay of the fracture intensity  $P_{21}$  with distance to the MSS ( $D$ ) and to subsidiary  $n$  structures ( $d_i$ ), modelled as a superposition of power-law functions corresponding to 1st and 2nd order faults. Labels correspond to CSL number. SSE: Standard square error, MAE: Mean Absolute Error.

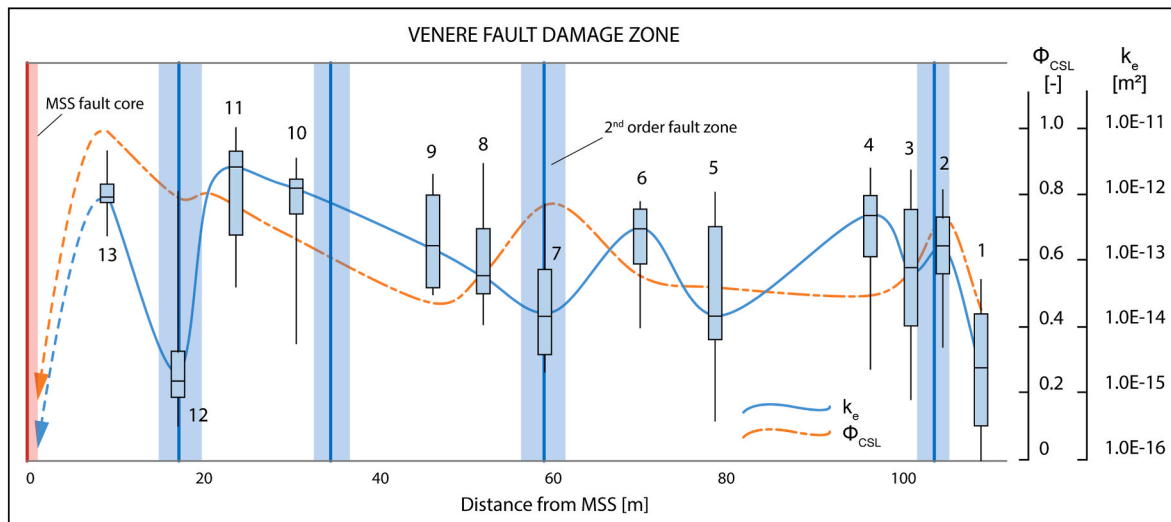


Fig. 10. Petrophysical properties measured on the CSL stations across the VF-DZ (Labels correspond to CSL number).  $\Phi_{CSL}$  is fracture porosity normalized with respect to the maximum value. Thus, the  $\Phi_{CSL}$  trend is independent of the applied aspect  $E/l$  ratio.  $k_e$  is equivalent fracture permeability and is shown by a box (limited by the 1st and 3rd quartile) and whisker plot in logarithmic scale, to illustrate its high variability across the damage zone. Red line is the location of the MSS, and blue lines are the locations of the 2nd order faults. (For interpretation of the references to colour in this figure legend, the reader is referred to the Web version of this article.)

modelled fracture intensity and porosity are lower than the values reported from the CSL analyses within the VF-DZ (Figs. 8 and 9). Therefore, we added a new fracture domain called weakly fractured carbonates, which is associated with the host rock of the VF zone. In this domain, the values of fracture intensity are almost stable (coefficient of variation  $<0.5\%$ ) and the fracture porosity (for  $E/l = 0.005$ ) is  $\sim 0.7\%$ .

Both the calculated density and seismic velocity should mimic the values of fracture porosity because they are derived from this parameter. However, as explained in section 3.2.3, the seismic velocities have a more complex relationship with fracture porosity (Kumar and Han, 2005). The calculated porosity, density, P-wave velocity, and the resultant reflectivity model of the GM2 fault zone model is shown in Fig. 11, and in tabulated format in Table 2.

#### 4.4. Seismic models

The geological and geophysical parameters adopted for the seismic modelling of the VF zone are summarized in section 3.3.1 (Fig. 5). The base model including the FDs distribution, fracture porosity and acoustic properties (Fig. 11 a-c) was tested, and a sensitivity analysis was applied to evaluate the (PSDM) seismic signature of the VF-DZ.

##### 4.4.1. Impact of geological parameters

To perform a sensitivity analysis based on different geological parameters, we use the 3 different geological models (GM1-3), which differ from each other in terms of surrounding lithologies (cf. Section 3.3.1, and Fig. 5). In general, we observe that only the FDs characterized by a higher fracture porosity variation (fragmented carbonates, and highly fractured carbonates) are visible in the seismic image due to their higher

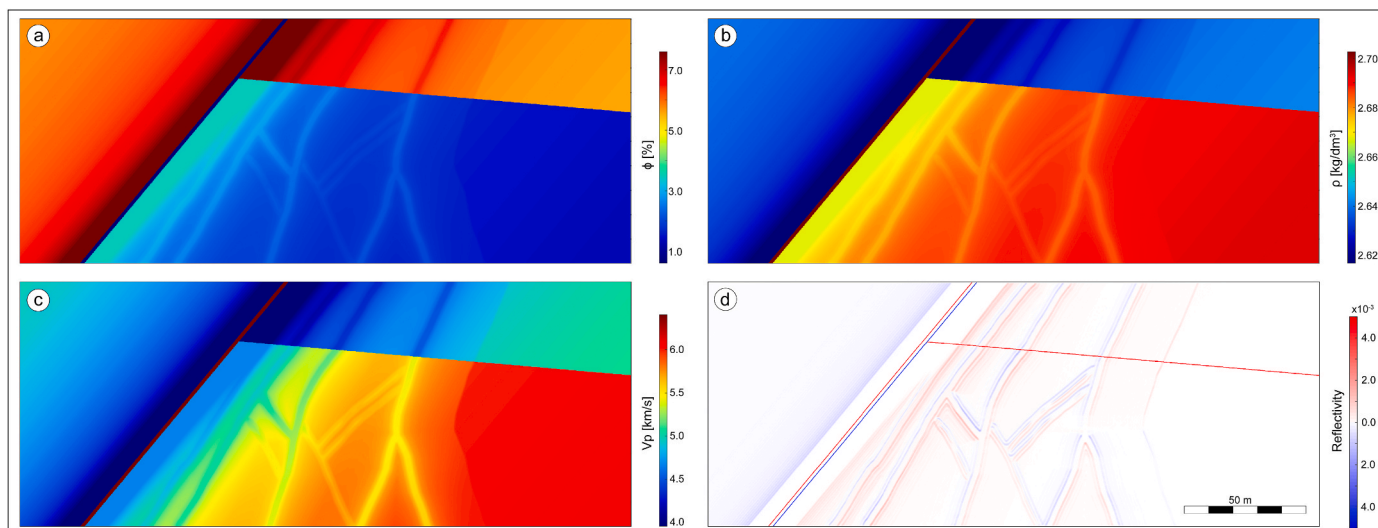


Fig. 11. a) Porosity ( $\phi$ ), b) Bulk density ( $\rho$ ), c) P-wave velocity ( $V_p$ ), and d) reflectivity of the GM2 base model, assuming an E/I ratio = 0.005.

Table 2

Summary of the modelled petrophysical and seismic velocity properties of the main fracture domains within the VF-DZ. Matrix porosity = 0.8% and fault core porosity = 0.6% according to Agosta et al. (2007). A second case considers a matrix porosity = 5.0%.

| Fracture Domain                    | E/I                  | $\phi$ [%]  |             |       | $V_p$ [km/s] |             |       | $V_s$ [km/s] |             |       | $\rho$ [g/cm <sup>3</sup> ] |             |       |
|------------------------------------|----------------------|-------------|-------------|-------|--------------|-------------|-------|--------------|-------------|-------|-----------------------------|-------------|-------|
|                                    |                      | 0.010       | 0.005       | 0.001 | 0.010        | 0.005       | 0.001 | 0.010        | 0.005       | 0.001 | 0.010                       | 0.005       | 0.001 |
| <b><math>\phi_m = 0.8\%</math></b> |                      |             |             |       |              |             |       |              |             |       |                             |             |       |
| Fragmented                         |                      | 6.20        | <b>3.50</b> | 1.34  | 3.45         | <b>4.67</b> | 6.07  | 1.81         | <b>2.46</b> | 3.20  | 2.63                        | <b>2.67</b> | 2.69  |
|                                    | Highly Fractured     | 5.20        | <b>3.00</b> | 1.24  | 3.87         | <b>4.92</b> | 6.12  | 2.04         | <b>2.59</b> | 3.22  | 2.65                        | <b>2.67</b> | 2.69  |
|                                    | Moderately Fractured | 4.00        | <b>2.40</b> | 1.12  | 4.43         | <b>5.32</b> | 6.19  | 2.33         | <b>2.80</b> | 3.26  | 2.66                        | <b>2.68</b> | 2.70  |
|                                    | Weakly Fractured     | 3.00        | <b>1.90</b> | 1.02  | 4.92         | <b>5.69</b> | 6.29  | 2.59         | <b>3.00</b> | 3.31  | 2.67                        | <b>2.69</b> | 2.70  |
|                                    |                      | 1.90        | <b>1.35</b> | 0.91  | 5.69         | <b>6.07</b> | 6.27  | 3.00         | <b>3.19</b> | 3.30  | 2.69                        | <b>2.69</b> | 2.70  |
| <b><math>\phi_m = 5.0\%</math></b> |                      |             |             |       |              |             |       |              |             |       |                             |             |       |
| Fragmented                         |                      | 10.40       | <b>7.70</b> | 5.54  | 3.02         | <b>3.96</b> | 5.15  | 1.59         | <b>2.08</b> | 2.71  | 2.58                        | <b>2.62</b> | 2.64  |
|                                    | Highly Fractured     | 9.40        | <b>7.20</b> | 5.44  | 3.29         | <b>4.19</b> | 5.23  | 1.73         | <b>2.21</b> | 2.75  | 2.60                        | <b>2.62</b> | 2.64  |
|                                    | Moderately Fractured | 8.20        | <b>6.60</b> | 5.32  | 3.74         | <b>4.47</b> | 5.32  | 1.97         | <b>2.36</b> | 2.80  | 2.61                        | <b>2.63</b> | 2.65  |
|                                    | Weakly Fractured     | 7.20        | <b>6.10</b> | 5.22  | 4.19         | <b>4.74</b> | 5.40  | 2.21         | <b>2.50</b> | 2.84  | 2.62                        | <b>2.64</b> | 2.65  |
|                                    |                      | 6.10        | <b>5.55</b> | 5.11  | 4.74         | <b>5.14</b> | 5.49  | 2.50         | <b>2.71</b> | 2.89  | 2.64                        | <b>2.64</b> | 2.65  |
| Fault core                         |                      | <b>0.60</b> |             |       | <b>6.43</b>  |             |       | <b>3.22</b>  |             |       | <b>2.64</b>                 |             |       |

impedance contrasts (Figs. 11 and 12). It is also clear that the area corresponding to the 2nd order fault farther from the MSS is not very visible. The internal architecture of the VF-DZ is imaged in more detail in model GM2 (Fig. 12b). Differently, in model GM1, the higher matrix porosity of the surrounding rocks provides a stronger reflector. Its seismic response masks the weaker reflection related to the reflector

near the MSS, which corresponds to the interface between the fragmented and highly fractured carbonates in the vicinity of the 2nd order fault closest to the MSS (Fig. 12a). This effect is more pronounced in model GM3 (Fig. 12c) due to an even higher impedance contrast because of the overlying flysch.

The fracture mechanical aperture, which is controlled by the fracture

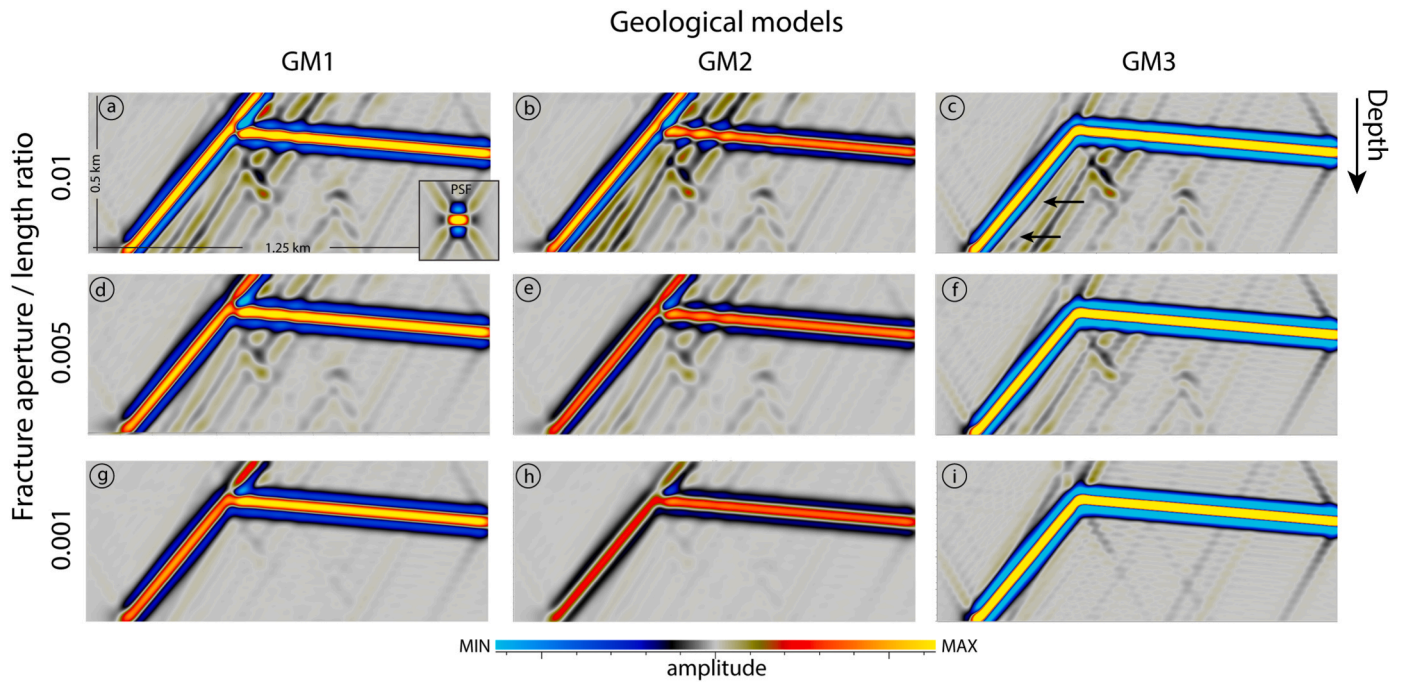


**Fig. 12.** Seismic signature of the VF-DZ for three different geological models (GM1 to GM3) and fracture aspect ratios ( $E/l = 0.01, 0.005$  and  $0.001$ ). (a, d, g) GM1 model, hanging wall and footwall overlying carbonates with 10% matrix porosity, (b, e, h) GM2 model, hanging wall and footwall overlying carbonates with 5% matrix porosity, (c, f, i) GM3 model, hanging wall and footwall overlying flysch. In all simulations, we use a 30 Hz dominant frequency and  $60^\circ$  illumination angle. The inset in (a) shows the PSF. The black arrows on c indicate the area with missing reflectors, masked by the seismic response of a stronger reflector related to the surrounding lithology.

aspect ratio  $E/l$ , significantly affects the imaging of the FDs within the VF-DZ. In the first scenario (high values of fracture aperture,  $E/l = 0.01$ ), the details of the internal architecture of the damage zone are highlighted by high amplitude reflectors that are stronger in the GM2 model, and weaker in the GM1 and GM3 models (Fig. 12a, b, and c). In the

second scenario (intermediate values of fracture aperture,  $E/l = 0.005$ ), the FDs' location and geometry are still recognizable from lower amplitude reflectors in all three GM models, although some details are lost (Fig. 12d, e, and f). Finally, in the third scenario (lowest fracture aperture,  $E/l = 0.001$ ), the FDs are not observable in any of the GM

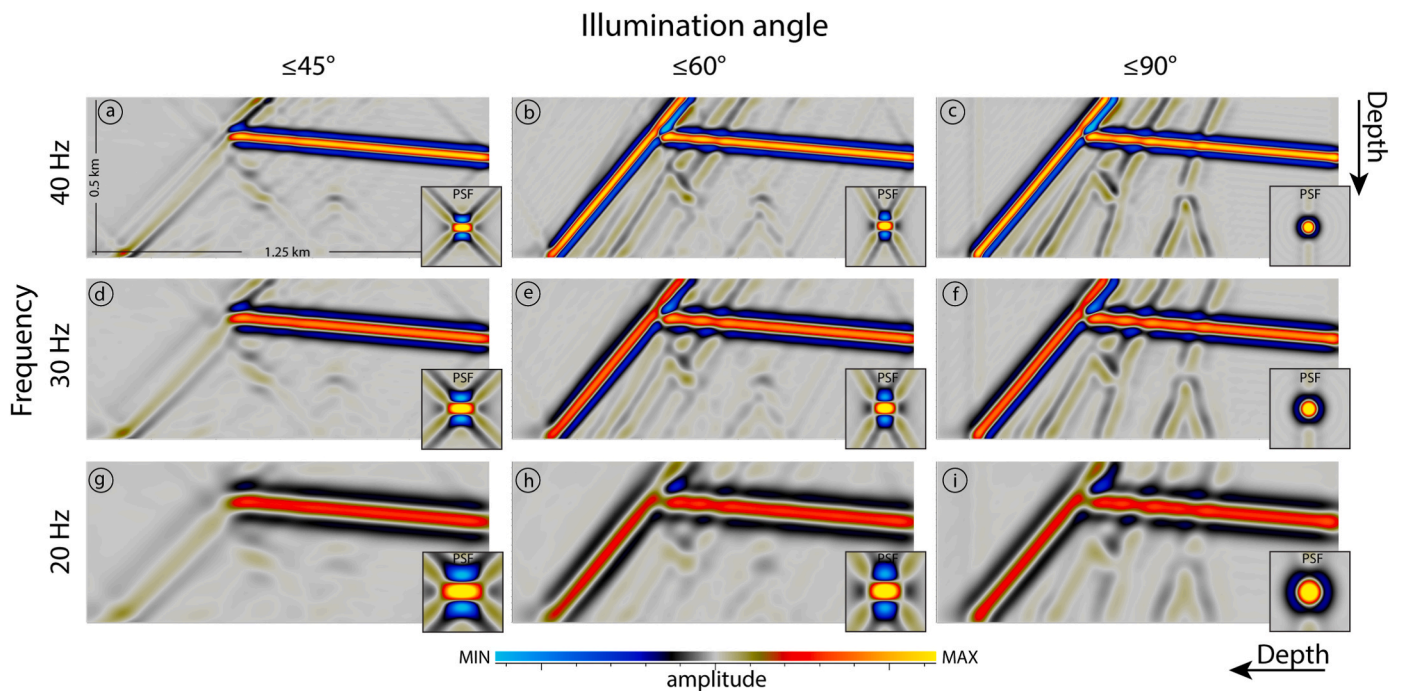


**Fig. 13.** Seismic signature of the VF-DZ for different illumination angles ( $45, 60$  and  $90^\circ$ , left to right) and dominant wavelet frequencies ( $40, 30$  and  $20$  Hz, top to bottom). The PSFs (insets) indicate the vertical and horizontal resolution of the seismic image. For this set of simulations, we used the middle-member case GM2 and  $E/l = 0.005$ .

models (Fig. 12g, h, and i).

#### 4.4.2. Effect of geophysical parameters

The aim of this section is to investigate the seismic signature of the VF-DZ by varying the maximum angle of illumination for dominant wavelet frequencies of 20, 30 and 40 Hz. We include only the results for the GM2 model and  $E/l = 0.005$ . The maximum illumination angles applied in this study are  $45^\circ$ ,  $60^\circ$ , and  $90^\circ$ , which correspond to intermediate (standard), high, and perfect seismic illuminations with the latter being in practice not attainable. The VF-DZ shows a great variation in seismic signature as the maximum illumination angle varies (Fig. 13). As expected, at perfect illumination ( $90^\circ$ ) the seismic signature of the VF-DZ shows illumination of the FDs related to the 2nd order faults (Fig. 13c, f, and i). At high illumination angle ( $60^\circ$ ), some details of the VF-DZ inner architecture are lost due to the lack of illumination of structures steeper than  $60^\circ$ . However, the FDs are still detectable on the seismic image, and can be partially interpreted (Fig. 13b, e, and h). On the contrary, the seismic sections modelled with a  $45^\circ$  maximum illumination angle do not show the MSS, and the FDs are only present as discontinuous/vanishing reflectors and seismic disturbance zones from antithetic structures with lower dip angle (Fig. 13a, d, and g). The decreasing dominant wavelet frequency clearly impacts the seismic image. This is particularly evident in the lowest frequency case (20 Hz, Fig. 13g, h, and i), where most details of the VF-DZ are lost resulting in a blurred seismic image.

## 5. Discussion

### 5.1. Fault damage zone architecture

The integration of observations and measurements on the outcrop and the virtual outcrop models allow us to obtain an accurate representation of the main structural complexity of the VF-DZ, specifically of both attitude and distribution of subsidiary faults. In agreement with Agosta and Aydin (2006), the MSS shows almost pure dip-slip kinematics, and minor right-lateral slip. The 2nd order faults are subparallel, and mainly synthetic to the MSS. Differently, the 3rd order faults show greater attitude variation, and cluster along the eastern wall close to the southern tip of the VF. Such a clustering is interpreted as due to along-strike kinematics variations associated with processes of lateral fault growth by segment linkage, as similarly documented for carbonate fault damage zones exposed in the northern edge of the Fucino Basin (Mercuri et al., 2020, and references therein).

The results of the CSL analyses are employed to calculate the main fracture parameters such as fracture density, P20, and intensity, P21. This procedure is an efficient tool for fracture distribution characterization in highly deformed carbonates and is relatively quicker than traditional time-consuming linear scanlines performed in carbonate fault damage zones (Panza et al., 2016, 2019; Zambrano et al., 2016; Giuffrida et al., 2019, 2020; Volatili et al., 2019).

We computed a composite power-law decay of fracture intensity from the MSS (cf. Fig. 9) within the VF-DZ. A similar composite fracture density decay has been documented for carbonate damage zones by Mayolle et al. (2019), where the effect of secondary faults is represented by the presence of secondary peaks in the fracture frequency decay function.

Although it is not possible to discern the actual contribution on fracture distribution by the 2nd order faults to the 1st order fault and vice versa, our field-based statistical approach (Fig. 9) demonstrate that the subsidiary fault zones farther from the MSS have higher peaks of fracture intensity with respect to the main fracture distribution decreasing trend. This behavior is likely linked to fault growth processes limited by an already fracture saturated environment approaching the MSS, yielding an obliteration of subsidiary fault damage zones.

### 5.2. Petrophysical properties

Previous studies on permeability distribution in carbonate fault damage zones based on different methods such as discrete fracture network modelling (Panza et al., 2018; Volatili et al., 2019, Romano et al., 2020, Smeraglia et al., 2021), in-situ measurements (Antonellini et al., 2014, Tondi et al., 2016; Riegel et al., 2019), laboratory tests of plugs derived from hand specimens (Bauer et al., 2016; Trippetta et al., 2017), and drill core samples and slug/injection tests (Westphal et al., 2004; Gabay et al., 2014) described a permeability range comprised between  $10^{-16}$  and  $10^{-11}$  m<sup>2</sup>. We show that the median values calculated in this work for fracture permeability vary from  $10^{-15}$  to  $10^{-12}$  m<sup>2</sup> across the VF-DZ (cf. Fig. 10). These values lie within the range above, and also highlight that the decreasing trend of the petrophysical properties moving away from the MSS present some divergencies near the 2nd order faults. This divergence is also shown in the poro-perm cross plot (Fig. 14). There, we document a power-law best-fit line ( $R^2 = 0.7$ ) of data gathered from CSL stations distant from 2nd order faults (blue dots in Fig. 14). We note that the aforementioned power-law poro-perm relation does not apply to data gathered in the vicinity of the 2nd order faults (orange squares in Fig. 14). We suggest two field-driven explanations for such behavior, causing a drastic reduction of fracture permeability independently of fracture porosity variation. First, within the most deformed zones (i.e., in proximity of the MSS and/or 2nd order faults), the fracture network is characterized by higher fracture intensity values, smaller fracture dimensions (i.e., length and aperture), and lower aspect ratios (fracture aperture-length relations shown in Fig. 8c) with respect to the surrounding network. Second, fractures aside the most deformed zones can be partially healed by carbonate cements, as documented along the 2nd order faults by Agosta and Aydin (2006). These authors reported the occurrence of sporadic veins clustering in the surrounding of slip surfaces bounding narrow pods of cataclastic rocks. In siliciclastic sedimentary successions, Riegel et al. (2019) also documented the control exerted by interconnected fracture networks on the cementation processes within fault damage zones. However, we note that an uneven distribution of fracture healing is predicted for active fault zones (Mizoguchi and Ueta, 2013), such as the studied VF-DZ.

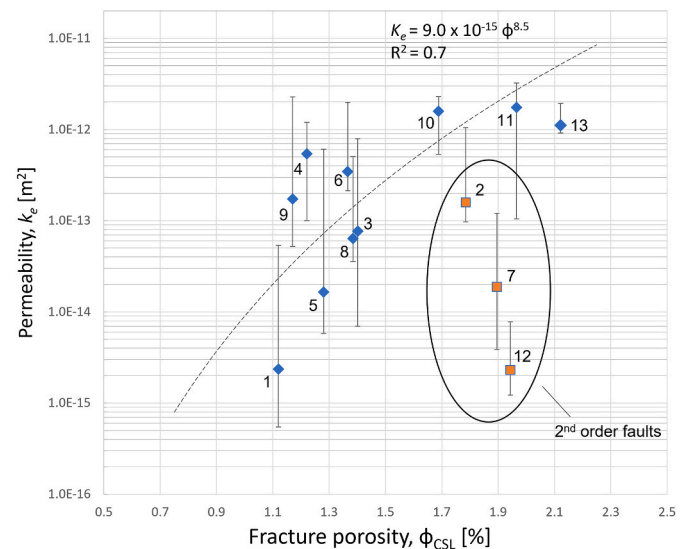


**Fig. 14.** Fracture porosity-permeability relationship. Labels correspond to CSL number. The dashed line corresponds to the power-law best-fit line of the CSL stations not affected by 2nd order faults (blue diamonds). The orange squares are stations on the 2nd order faults. The error bars stand for the first and third quartile of the equivalent permeability ( $k_e$ ).  $\Phi_{CSL}$  is determined from a 0.005  $E/l$  aspect ratio for reference. (For interpretation of the references to colour in this figure legend, the reader is referred to the Web version of this article.)

### 5.3. Seismic modelling

Several studies document the benefit of using field-based geological models as input data for seismic modeling (i.e., [Rabbel et al., 2018](#); [Grippa et al., 2019](#); [Wrona et al., 2020](#)). This procedure helps unraveling the seismic response of complex stratigraphy and structural heterogeneities. Some works have used digital outcrop models for seismic modelling ([Anell et al., 2016](#); [Lubrano-Lavadera et al., 2019](#)). In this contribution, the use of an integrated field- and digital-based model of the VF-DZ allows the investigation of the seismic signature of a complex fault architecture by considering various geological and geophysical parameters. In fact, despite the lack of model constraints such as well-log data, survey geometry, and background velocity, the versatility offered by the PSF-based convolution modelling technique allows us to perform a sensitivity analysis of the (PSDM) seismic signature of the VF zone ([Figs. 12 and 13](#)).

According to the results, the first set of simulations, investigating the effect of geological parameters while keeping the same geophysical parameters ([Fig. 12](#)), shows a slight obliteration of the internal architecture of the VF-DZ by the masking effect of the strong and regular reflectors in the GM1 to GM3 models. This means that the surrounding lithology does not significantly affect the seismic imaging of the VF-DZ. Conversely, the fracture mechanical aperture seems to be a crucial parameter. In fact, the sensitivity analysis based on the fracture aspect ratio ( $E/l$ ) demonstrates that the fault architecture is not imaged in the low-end case ( $E/l = 0.001$ ), thus suggesting that if fracture porosity is below 1%, due to very small average fracture aperture (few microns), their FDs would not give high enough impedance contrasts to be imaged on seismic. The latter fracture aspect ratio scenario is the most representative for km-depth structures affected by very high confining pressure (e.g., >50 MPa), returning fracture aperture values in the order of few microns, thus consistent with a well-known fracture aperture reduction due to overburden load ([Nelson and Handin, 1977](#)).

The second set of simulations investigating the effect of geophysical parameters ([Fig. 13](#)) while keeping the same geological parameters, i.e., the middle-member case GM2 and  $E/l = 0.005$  of [Fig. 12](#), identify the 30 Hz dominant frequency as the lowest frequency required to image the internal architecture of the VF-DZ, without losing details depicting the FDs. However, since the model of the fault zone was enlarged five times to simulate reasonable dominant frequencies commonly observed in conventional seismic at km depth (i.e., 20, 30, and 40 Hz), this means that a much higher frequency typical of high-resolution seismic data (i.e., ~150 Hz) is required to image the fault zone in its actual size. In this regard, [Faleide et al. \(2021\)](#), comparing conventional and high-resolution seismic data, pointed out the need of coupling the latter with seismic modelling to reduce uncertainties related to seismic interpretation of fault zones. Similarly, the illumination angle, which in an actual seismic survey is determined by the background velocity model and a given survey geometry, shows how the steepest features (i.e., MSS and 2nd order faults) are barely imaged by illumination angles below 45° ([Fig. 13a, d, g](#)). At standard or low illumination angles (and larger depths), the fault would only be detected by the vertical offset of gently dipping reflectors. Therefore, the left cases of [Fig. 13](#), where the fault plane does not appear due to lack of illumination, would likely represent the outcomes of conventional seismic at km-depths. This suggests that the complex internal architecture of structures like the VF-DZ at km-depth would be mostly undetected by conventional seismic, although their presence and related petrophysical heterogeneity, as documented in this study, may affect fluid flow. However, the seismic signature of the VF-DZ will still be characterized by the occurrence of seismic disturbance zones related to the subsidiary structures. Through seismic modelling, [Faleide \(2021\)](#) reported the occurrence of similar disturbances of the seismic signal in a fault damage zone.

## 6. Conclusions

We presented a multidisciplinary integrated characterization of a seismic scale (throw  $\approx 300$  m) normal fault zone, the Venere Fault (VF), which cuts across Upper Jurassic-Lower Cretaceous platform carbonates and bounds the eastern side of the Fucino Basin (central Italy). The VF damage zone (VF-DZ) architecture was investigated from the structural, petrophysical, and seismic imaging points of view. By combining field- and digital-based structural analyses, the results highlight the profound control exerted by subsidiary faults on both fracture distribution and petrophysical properties. The resultant 2D model of the VF-DZ was then populated with elastic properties (i.e.,  $V_p$ ,  $V_s$  and density values) derived from the porosity of both the matrix and fracture components. This base model depicting subsidiary structures that impart heterogeneity to the fault zone, was the input to seismic modelling that allowed us to perform a sensitivity analysis according to various geological (surrounding lithology and fracture aperture) and geophysical parameters (wave frequency and illumination angle). To test the impact of a structure like the VF-DZ at km-depths and with standard seismic frequencies (~20–40 Hz) the model was enlarged five times. The main outcomes of this work are the following:

- In terms of deformation, fracture abundance distribution does not decrease regularly away from the main slip surface (MSS). In contrast, the fracture distribution is profoundly affected by the occurrence of subsidiary faults. In this regard, we documented a composite power-law decay of fracture intensity as a function of the distance from the MSS and the single secondary faults.
- Regarding petrophysical properties, both fracture porosity and permeability show a decreasing trend away from the MSS. However, they are also profoundly affected by subsidiary faults. In fact, the computed fracture porosity increases by a factor of 2–3, whereas permeability decreases down to 3 orders of magnitude near subsidiary faults.
- From seismic imaging, we can assess that the most relevant geological parameter affecting the seismic signature of the VF-DZ is fracture aperture. When this parameter yields fracture porosity values below 1%, the internal architecture of the damage zone is not visible on seismic. Higher impedance contrasts by different surrounding lithologies slightly conceal the reflectors close to the MSS, without drastically compromising the VF-DZ signal.
- High frequencies (~150 Hz) are required to image the VF-DZ in its actual size. The same fault model enlarged five times, requires a minimum frequency of 30 Hz to be properly imaged. The illumination angle strongly influences the seismic image. In conventional seismic at km-depth (illumination angle  $\leq 45^\circ$ ) the subsidiary structures within the VF-DZ are partially imaged as seismic disturbance zones but most of the details are lost.

The applied methodology is greatly adaptable to different geologic settings. Coupling petrophysical outcrop-based models with seismic modelling can improve the seismic interpretation and characterization of fault zones. In particular, the observed variations of fracture abundance along subsidiary structures in outcrop can be simulated on seismic images by using various geological and geophysical scenarios. This is of particular interest for reservoir characterization in carbonates, where the heterogeneity of fracture density/intensity given by subsidiary faults or fracture corridors play a crucial role on the fluid storage and migration properties of large-scale fault zones.

### Author statement

**Tiziano Volatili:** Conceptualization, Methodology, Formal analysis, Investigation, Data curation, Writing – Original draft, Visualization.

**Fabrizio Agosta:** Conceptualization, Methodology, Writing – Review & Editing.

**Nestor Cardozo:** Conceptualization, Methodology, Writing – Review & Editing.

**Miller Zambrano:** Methodology, Formal analysis, Writing – Review & Editing.

**Isabelle Lecomte:** Methodology, Writing – Review & Editing.

**Emanuele Tondi:** Writing – Review & Editing, Supervision, Funding acquisition.

## Declaration of competing interest

The authors declare that they have no known competing financial interests or personal relationships that could have appeared to influence the work reported in this paper.

## Acknowledgements

Data reported in this manuscript are part of the first author's PhD Thesis Dissertation. The core of the manuscript was written during an Erasmus visit of the first author to the University of Stavanger. Mr. Santilli is warmly thanked for providing us free access to the studied quarry. Fabrizio Balsamo (University of Parma) is acknowledged for the portable air permeameter employed during outcrop analysis. Francesco Ferraro is also acknowledged for the help provided in the field during the first circular scanline measurements. Furthermore, we thank NOR-SAR Innovation for providing an academic license of SeisRoX Pro 2019. This research was funded by the Reservoir Characterization Project ([www.rechproject.com](http://www.rechproject.com)) and the FAR Unicum project "Novel Approach for Seismic Hazard Analysis—NoHAR".

## References

- Agosta, F., Kirschner, D.L., 2003. Fluid conduits in carbonate-hosted seismogenic normal faults of central Italy. *J. Geophys. Res. Solid Earth* 108 (B4).
- Agosta, F., Aydin, A., 2006. Architecture and deformation mechanism of a basin-bounding normal fault in Mesozoic platform carbonates, central Italy. *J. Struct. Geol.* 28 (8), 1445–1467.
- Agosta, F., Prasad, M., Aydin, A., 2007. Physical properties of carbonate fault rocks, fucino basin (Central Italy): implications for fault seal in platform carbonates. *Geofluids* 7 (1), 19–32.
- Agosta, F., 2008. Fluid flow properties of basin-bounding normal faults in platform carbonates. Fucino Basin, central Italy. Geological Society, London, Special Publications 299 (1), 277–291.
- Alaie, B., Torabi, A., 2017. Seismic imaging of fault damaged zone and its scaling relation with displacement. *Interpretation* 5 (4), SP83–SP93.
- Anders, M.H., Wiltschko, D.V., 1994. Microfracturing, paleostress and the growth of faults. *J. Struct. Geol.* [https://doi.org/10.1016/0191-8141\(94\)90146-5](https://doi.org/10.1016/0191-8141(94)90146-5).
- Anelli, L., Lecomte, I., Braathen, A., Buckley, S.J., 2016. Synthetic seismic illumination of small-scale growth faults, paralic deposits and low-angle clinoforms: a case study of the Triassic successions on Edgeøya, NW Barents Shelf. *Mar. Petrol. Geol.* <https://doi.org/10.1016/j.marpetgeo.2016.07.005>.
- Antonellini, M., Cilona, A., Tondi, E., Zambrano, M., Agosta, F., 2014. Fluid flow numerical experiments of faulted porous carbonates, Northwest Sicily (Italy). *Mar. Petrol. Geol.* <https://doi.org/10.1016/j.marpetgeo.2013.12.003>.
- Aydin, A., 2000. Fractures, faults, and hydrocarbon entrapment, migration and flow. *Mar. Petrol. Geol.* [https://doi.org/10.1016/S0264-8172\(00\)00020-9](https://doi.org/10.1016/S0264-8172(00)00020-9).
- Balsamo, F., Storti, F., Salvini, F., Silva, A.T., Lima, C.C., 2010. Structural and petrophysical evolution of extensional fault zones in low-porosity, poorly lithified sandstones of the Barreiras Formation, NE Brazil. *J. Struct. Geol.* <https://doi.org/10.1016/j.jsg.2009.10.010>.
- Bauer, H., Schröckenfuchs, T.C., Decker, K., 2016. Hydrogeological properties of fault zones in a karstified carbonate aquifer (Northern Calcareous Alps, Austria). *Hydrogeol. J.* 24 (5), 1147–1170.
- Bigi, G., Cosentino, D., Parotto, M., Sartori, R., Scandone, P., 1992. Structural Model of Italy, scale 1:500,000, 6 sheets. CNR, Quaderni di Ricerca Scientifica 114.
- Boschi, E., Guidoboni, E., Ferrari, G., Valensise, G., 1997. In: *Catalogo dei forti terremoti in Italia dal 461 A.C. al 1990*. ING-SGA, p. 644.
- Botter, C., Cardozo, N., Hardy, S., Lecomte, I., Escalona, A., 2014. From mechanical modeling to seismic imaging of faults: a synthetic workflow to study the impact of faults on seismic. *Mar. Petrol. Geol.* <https://doi.org/10.1016/j.marpetgeo.2014.05.013>.
- Botter, C., Cardozo, N., Hardy, S., Lecomte, I., Paton, G., Escalona, A., 2016. Seismic characterisation of fault damage in 3D using mechanical and seismic modelling. *Mar. Petrol. Geol.* <https://doi.org/10.1016/j.marpetgeo.2016.08.002>.
- Botter, C., Cardozo, N., Qu, D., Tveranger, J., Kolyukhin, D., 2017. Seismic characterization of fault facies models. *Interpretation.* <https://doi.org/10.1190/int-2016-0226.1>.
- Caine, J.S., Evans, J.P., Forster, C.B., 1996. Fault zone architecture and permeability structure. *Geology.* [https://doi.org/10.1130/0091-7613\(1996\)024<1025:FZAAPS>2.3.CO;2](https://doi.org/10.1130/0091-7613(1996)024<1025:FZAAPS>2.3.CO;2).
- Camanni, G., Vinci, F., Tavani, S., Ferrandino, V., Mazzoli, S., Corradetti, A., Parente, M., Iannace, A., 2021. Fracture density variations within a reservoir-scale normal fault zone: a case study from shallow-water carbonates of southern Italy. *J. Struct. Geol.* 151, 104432.
- Cavinato, G.P., Carusi, C., Dall'asta, M., Miccadei, E., Piacentini, T., 2002. Sedimentary and tectonic evolution of Plio-Pleistocene alluvial and lacustrine deposits of Fucino Basin (central Italy). *Sediment. Geol.* [https://doi.org/10.1016/S0037-0738\(01\)00209-3](https://doi.org/10.1016/S0037-0738(01)00209-3).
- Ceccato, A., Viola, G., Antonellini, M., Tartaglia, G., Ryan, E.J., 2021. Constraints upon fault zone properties by combined structural analysis of virtual outcrop models and discrete fracture network modelling. *J. Struct. Geol.* 152, 104444.
- Chopra, S., Marfurt, K.J., 2009. Interpreting fractures through 3D seismic discontinuity attributes and their visualization. *CSEG Recorder* 34 (8), 5–14.
- Cohen, I., Coult, N., Vassiliou, A.A., 2006. Detection and extraction of fault surfaces in 3D seismic data. *Geophysics.* <https://doi.org/10.1190/1.2215357>.
- Cowie, P.A., Scholz, C.H., 1992. Growth of faults by accumulation of seismic slip. *J. Geophys. Res. Solid Earth* 97 (B7), 11085–11095.
- Cunningham, J., Cardozo, N., Townsend, C., Iacopini, D., Waerum, G.O., 2019. Fault deformation, seismic amplitude and unsupervised fault facies analysis: Snøhvit Field, Barents Sea. *J. Struct. Geol.* 118, 165–180.
- Davatzes, N.C., Aydin, A., 2003. Overprinting faulting mechanisms in high porosity sandstones of SE Utah. *J. Struct. Geol.* 25 (11), 1795–1813.
- De Jossineau, G., Aydin, A., 2007a. The evolution of the damage zone with fault growth in sandstone and its multiscale characteristics. *J. Geophys. Res. Solid Earth* 112 (B12).
- De Jossineau, G., Mutlu, O., Aydin, A., Pollard, D., 2007b. Characterization of fault-splay relationships: field survey and mechanical modeling. *J. Struct. Geol.* 29, 1831–1842.
- Dutzer, J.F., Basford, H., Purves, S., 2010. Investigating fault-sealing potential through fault relative seismic volume analysis. In: *Petroleum Geology Conference Proceedings.* <https://doi.org/10.1144/0070509>.
- Faleide, T.S., Braathen, A., Lecomte, I., Mulrooney, M.J., Midtkandal, I., Bugge, A.J., Planke, S., 2021. Impacts of seismic resolution on fault interpretation: insights from seismic modelling. *Tectonophysics* 816, 229008.
- Faleide, T.S., 2021. Seismic Imaging of Faults and Sedimentary Systems of the Hoop Region, Barents Sea: Seismic Facies, Fault Geometries and Detection Thresholds. Series of Dissertations Submitted to the Faculty of Mathematics and Natural Sciences. ISSN 1501-7710. University of Oslo. No. 2450.
- Faulkner, D.R., Mitchell, T.M., Healy, D., Heap, M.J., 2006. Slip on "weak" faults by the rotation of regional stress in the fracture damage zone. *Nature.* <https://doi.org/10.1038/nature05353>.
- Faulkner, D.R., Mitchell, T.M., Jensen, E., Cembrano, J., 2011. Scaling of fault damage zones with displacement and the implications for fault growth processes. *J. Geophys. Res. Solid Earth* 116 (B5).
- Faure Walker, J.P., Roberts, G.P., Sammonds, P.R., Cowie, P., 2010. Comparison of earthquake strains over 102 and 104 year timescales: insights into variability in the seismic cycle in the central Apennines, Italy. *J. Geophys. Res.* 115, B10418. <https://doi.org/10.1029/2009JB006462>.
- Ferraro, F., Grieco, D.S., Agosta, F., Prosser, G., 2018. Space-time evolution of cataclasis in carbonate fault zones. *J. Struct. Geol.* 110, 45–64.
- Ferraro, F., Agosta, F., Ukar, E., Grieco, D.S., Cavalcante, F., Belviso, C., Prosser, G., 2019. Structural diagenesis of carbonate fault rocks exhumed from shallow crustal depths: an example from the central-southern Apennines, Italy. *J. Struct. Geol.* 122, 58–80.
- Ferraro, F., Agosta, F., Prasad, M., Vinciguerra, S., Violay, M., Giorgioni, M., 2020. Pore space properties in carbonate fault rocks of peninsular Italy. *J. Struct. Geol.* <https://doi.org/10.1016/j.jsg.2019.103913>.
- Filomena, C.M., Hornung, J., Stollhofen, H., 2014. Assessing accuracy of gas-driven permeability measurements: a comparative study of diverse Hassler-cell and probe permeameter devices. *Solid Earth.* <https://doi.org/10.5194/se-5-1-2014>.
- Fossen, H., Gabrielsen, R.H., 1996. Experimental modeling of extensional fault systems by use of plaster. *J. Struct. Geol.* 18 (5), 673–687.
- Gabay, R., Eyal, S., Yoseph, Y., Amir, S., Noam, W., 2014. The permeability of fault zones: a case study of the Dead Sea rift (Middle East). *Hydrogeol. J.* 22, 425–440.
- Galadini, F., Galli, P., 1999. The Holocene paleo-earthquakes on the 1915 Avezzano earthquake faults (central Italy): implications for active tectonics in the central Apennines. *Tectonophysics* 308, 143e170.
- Ghanbarian, B., Perfect, E., Liu, H.H., 2019. A geometrical aperture-width relationship for rock fractures. *Fractals* 27 (1), 1940002.
- Ghiesetti, F., Vezzani, L., 1999. Depth and modes of Pliocene-Pleistocene crustal extension of the Apennines (Italy). *Terra. Nova* 11, 67e72.
- Ghiesetti, F., Kirschner, D.L., Vezzani, L., Agosta, F., 2001. Stable isotope evidence for contrasting paleofluid circulation in thrust and seismogenic normal faults of central Apennines, Italy. *J. Geophys. Res.* 106, 8811–8825.
- Ghiesetti, F., Vezzani, L., 2002. Normal faulting, extension and uplift in the outer thrust belt of the central Apennines (Italy): role of the Caramanico fault. *Basin Res.* 14 (2), 225–236.
- Giuffrida, A., Agosta, F., Rustichelli, A., Panza, E., La Bruna, V., Eriksson, M., Torrieri, S., Giorgioni, M., 2020. Fracture stratigraphy and DFN modelling of tight carbonates, the case study of the Lower Cretaceous carbonates exposed at the Monte Alpi (Basilicata, Italy). *Mar. Petrol. Geol.* <https://doi.org/10.1016/j.marpetgeo.2019.104045>.

- Giuffrida, A., La Bruna, V., Castelluccio, P., Panza, E., Rustichelli, A., Tondi, E., Giorgioni, M., Agosta, F., 2019. Fracture simulation parameters of fractured reservoirs: analogy with outcropping carbonates of the Inner Apulian Platform, southern Italy. *J. Struct. Geol.* <https://doi.org/10.1016/j.jsg.2019.02.007>.
- Grippa, A., Hurst, A., Palladino, G., Iacopini, D., Lecomte, I., Huuse, M., 2019. Seismic imaging of complex geometry: forward modeling of sandstone intrusions. *Earth Planet Sci. Lett.* <https://doi.org/10.1016/j.epsl.2019.02.011>.
- Gudmundsson, A., Berg, S.S., Lyslo, K.B., Skurtveit, E., 2001. Fracture networks and fluid transport in active fault zones. *J. Struct. Geol.* [https://doi.org/10.1016/S0191-8141\(00\)00100-0](https://doi.org/10.1016/S0191-8141(00)00100-0).
- Iacopini, D., Butler, R.W.H., Purves, S., McArdle, N., De Freslon, N., 2016. Exploring the seismic expression of fault zones in 3D seismic volumes. *J. Struct. Geol.* <https://doi.org/10.1016/j.jsg.2016.05.005>.
- James, M.R., Robson, S., 2012. Straightforward reconstruction of 3D surfaces and topography with a camera: accuracy and geoscience application. *J. Geophys. Res.: Earth Surf.* 117 (F3).
- Johri, M., Zoback, M.D., Hennings, P., 2014. A scaling law to characterize fault-damage zones at reservoir depths. *AAPG (Am. Assoc. Pet. Geol.) Bull.* 98 (10), 2057–2079.
- Klimczak, C., Schultz, R.A., Parashar, R., Reeves, D.M., 2010. Cubic law with aperture-length correlation: implications for network scale fluid flow. *Hydrogeol. J.* 18 (4), 851–862.
- Kumar, M., Han, D.H., 2005. Pore shape effect on elastic properties of carbonate rocks. In: *SEG Technical Program Expanded Abstracts 2005*. Society of Exploration Geophysicists, pp. 1477–1480.
- Lanari, R., Faccenna, C., Benedetti, L., Sembroni, A., Bellier, O., Menichelli, I., Primerano, P., Molin, P., 2021. Formation and persistence of extensional internally drained basins: the case of the Fucino basin (Central Apennines, Italy). *Tectonics* 40. <https://doi.org/10.1029/2020TC006442> e2020TC006442.
- Lasdon, L.S., Fox, R.L., Ratner, M.W., 1974. Nonlinear optimization using the generalized reduced gradient method. *Revue française d'automatique, informatique, recherche opérationnelle. Recherche opérationnelle* 8 (V3), 73–103.
- Lecomte, I., 2008. Resolution and Illumination Analyses in PSDM: A Ray-Based Approach. *Leading Edge*, Tulsa, OK. <https://doi.org/10.1190/1.2919584>.
- Lecomte, I., Kaschwich, T., 2018. Closer to real earth in reservoir characterization: a 3D isotropic/anisotropic PSDM simulator. In: *78th Society of Exploration Geophysicists International Exposition and Annual Meeting*. SEG 2008.
- Lecomte, I., Lavadera, P.L., Anell, I., Buckley, S.J., Schmid, D.W., Heeremans, M., 2015. Ray-based Seismic Modeling of Geologic Models: Understanding and Analyzing Seismic Images Efficiently. <https://doi.org/10.1190/INT-2015-0061.1>. Interpretation.
- Lecomte, I., Lavadera, P.L., Botter, C., Anell, I., Buckley, S.J., Eide, C.H., Grippa, A., Mascolo, V., Kjøberg, S., 2016. 2(3)D Convolution Modelling of Complex Geological Targets beyond – 1D Convolution. *First Break*.
- Li, F., Zhao, T., Lin, T., Marfurt, K.J., 2015. Fracture characterization based on attenuation estimation from seismic reflection data using well-log-based localized spectral correction. In: *Society of Petroleum Engineers - Unconventional Resources Technology Conference*. <https://doi.org/10.2118/178529-ms>. URTEC 2015.
- Liao, Z., Liu, H., Carpenter, B.M., Marfurt, K.J., Reches, Z., 2019. Analysis of fault damage zones using three-dimensional seismic coherence in the Anadarko Basin, Oklahoma. *AAPG (Am. Assoc. Pet. Geol.) Bull.* <https://doi.org/10.1306/1219181413417207>.
- Lubrano-Lavadera, P., Senger, K., Lecomte, I., Mulrooney, M.J., Kühn, D., 2019. Seismic modelling of metre-scale normal faults at a reservoir-cap rock interface in central spitsbergen, svalbard: implications for CO<sub>2</sub> storage. *Nor. Geol. Tidsskr.* <https://doi.org/10.17850/njg003>.
- Mauldon, M., Dunne, W.M., Rohrbaugh, M.B., 2001. Circular scanlines and circular windows: new tools for characterizing the geometry of fracture traces. *J. Struct. Geol.* [https://doi.org/10.1016/S0191-8141\(00\)00094-8](https://doi.org/10.1016/S0191-8141(00)00094-8).
- Mayolle, S., Soliva, R., Caniven, Y., Wibberley, C., Ballas, G., Dominguez, S., Milési, G., 2019. Scaling of fault damage zones and implications for naturally fractured reservoirs, 1. In: *Fifth International Conference on Fault and Top Seals*. European Association of Geoscientists & Engineers, pp. 1–5, 2019.
- Mayolle, S., Soliva, R., Dominguez, S., Wibberley, C., Caniven, Y., 2021. Nonlinear fault damage zone scaling revealed through analog modeling. *Geology*.
- Mancinelli, P., Scisciani, V., Patruno, S., Minelli, G., 2021. Gravity modeling reveals a Messinian foredeep depocenter beneath the intermontane Fucino Basin (central Apennines). *Tectonophysics* 821, 229144.
- Mendez, J.N., Jin, Q., Gonzalez, M., Zhang, X., Lobo, C., Boateng, C.D., Zambrano, M., 2020. Fracture characterization and modeling of karsted carbonate reservoirs: a case study in Tahe oilfield, Tarim Basin (western China). *Mar. Petrol. Geol.* 112, 104104.
- Mercuri, M., McCaffrey, K.J.W., Smeraglia, L., Mazzanti, P., Collettini, C., Carminati, E., 2020. Complex geometry and kinematics of subsidiary faults within a carbonate-hosted relay ramp. *J. Struct. Geol.* <https://doi.org/10.1016/j.jsg.2019.103915>.
- Merico, A., Jezi, G., Pace, B., Ferranti, L., Cremona, M., Scafa, M., Cavallo, A., Colella, A., Nazzari, M., Scarlati, P., 2020. Grain size and grain size distribution of a lithified fault core in carbonates rocks using multi-scale image analysis: the example of the San Benedetto-Gioia dei Marsi fault (Central Italy). *J. Struct. Geol.* 134, 104017.
- Michelena, R.J., Godbey, K.S., Wang, H., Oilman, J.R., Zahm, C.K., 2013. Estimation of Dispersion in Orientations of Natural Fractures from Seismic Data: Application to DFN Modeling and Flow Simulation. <https://doi.org/10.1190/tle32121502.1>. *Leading Edge*.
- Michetti, A.M., Brunamonte, F., Serva, L., Vittori, E., 1996. Trench investigations of the 1915 Fucino earthquake fault scarps (Abruzzo, Central Italy): geological evidence of large historical events. *J. Geophys. Res. Solid Earth* 101 (B3), 5921–5936.
- Miller, S.L., 1992. Well log analysis of Vp and vs in carbonates. *Consurtium for Research in Elastic Wave Explor. Seismol. (CREWES) Res. Rep.* 4, 1–12.
- Mitchell, T.M., Faulkner, D.R., 2009. The nature and origin of off-fault damage surrounding strike-slip fault zones with a wide range of displacements: a field study from the Atacama fault system, northern Chile. *J. Struct. Geol.* <https://doi.org/10.1016/j.jsg.2009.05.002>.
- Mizoguchi, K., Ueta, K., 2013. Microfractures within the fault damage zone record the history of fault activity. *Geophys. Res. Lett.* 40 (10), 2023–2027.
- Myers, R., Aydin, A., 2004. The evolution of faults formed by shearing across joint zones in sandstone. *J. Struct. Geol.* 26 (5), 947–966.
- Nelson, R.A., Handin, J., 1977. Experimental study of fracture permeability in porous rock. *AAPG (Am. Assoc. Pet. Geol.) Bull.* 61 (2), 227–236.
- Olson, J.E., 2003. Sublinear scaling of fracture aperture versus length: an exception or the rule? *J. Geophys. Res. Solid Earth* 108 (B9).
- Panza, E., Agosta, F., Rustichelli, A., Zambrano, M., Tondi, E., Prosser, G., Giorgioni, M., Janisek, J.M., 2016. Fracture stratigraphy and fluid flow properties of shallow-water, tight carbonates: the case study of the Murge Plateau (southern Italy). *Mar. Petrol. Geol.* 73, 350–370.
- Panza, E., Agosta, F., Vinciguerra, S.C., Ougier-Simonin, A., Dobbs, M., Prosser, G., 2019. Meso-to-microscale fracture porosity in tight limestones, results of an integrated field and laboratory study. *Mar. Petrol. Geol.* <https://doi.org/10.1016/j.marpetgeo.2019.01.043>.
- Panza, E., Sessa, E., Agosta, F., Giorgioni, M., 2018. Discrete Fracture Network modelling of a hydrocarbon-bearing, oblique-slip fault zone: inferences on fault-controlled fluid storage and migration properties of carbonate fault damage zones. *Mar. Petrol. Geol.* <https://doi.org/10.1016/j.marpetgeo.2017.09.009>.
- Patruno, S., Scisciani, V., 2021. Testing normal fault growth models by seismic stratigraphic architecture: the case of the Pliocene-Quaternary Fucino Basin (Central Apennines, Italy). *Basin Res.* 33 (3), 2118–2156.
- Piccardi, L., Gaudemer, Y., Tapponnier, P., Boccaletti, M., 1999. Active oblique extension in the central Apennines (Italy): evidence from the Fucino region. *Geophys. J. Int.* 2, 499–530.
- Pitts, A.D., Casciano, C.I., Patacci, M., Longhitano, S.G., Di Celma, C., McCaffrey, W.D., 2017. Integrating traditional field methods with emerging digital techniques for enhanced outcrop analysis of deep water channel-fill deposits. *Mar. Petrol. Geol.* <https://doi.org/10.1016/j.marpetgeo.2017.05.001>.
- Rabbell, O., Galland, O., Mair, K., Lecomte, I., Senger, K., Spacapan, J.B., Manceda, R., 2018. From field analogues to realistic seismic modelling: a case study of an oil-producing andesitic sill complex in the Neuquén Basin, Argentina. *J. Geol. Soc.* <https://doi.org/10.1144/jgs2017-116>.
- Riegel, H., Zambrano, M., Balsamo, F., Mattioni, L., Tondi, E., 2019. Petrophysical properties and microstructural analysis of faulted heterolithic packages: a case study from Miocene turbidite successions. Italy. *Geofluids*. <https://doi.org/10.1155/2019/9582359>.
- Roberts, G.P., Michetti, A.M., 2004. Spatial and temporal variations in growth rates along active normal fault systems: an example from the Lazio-Abruzzo Apennines, central Italy. *J. Struct. Geol.* 26 (2), 339–376.
- Rohrbaugh, J.B., Dunne, W.M., Mauldon, M., 2002. Estimating fracture trace intensity, density, and mean length using circular scan lines and windows. *AAPG (Am. Assoc. Pet. Geol.) Bull.* <https://doi.org/10.1306/61eede0e-173e-11d7-8645000102c1865d>.
- Romano, V., Bigi, S., Carnevale, F., De Haven Hyman, J., Karra, S., Valocchi, A.J., Tartarello, M.C., Battaglia, M., 2020. Hydraulic characterization of a fault zone from fracture distribution. *J. Struct. Geol.* <https://doi.org/10.1016/j.jsg.2020.104036>.
- Rotevatn, A., Fossen, H., Hesthammer, J., Aas, T.E., Howell, J.A., 2007. Are Relay Ramps Conduits for Fluid Flow? Structural Analysis of a Relay Ramp in Arches National Park, Utah. *Geological Society Special Publication*. <https://doi.org/10.1144/GSL.SP.2007.270.01.04>.
- Sagy, A., Reches, Z.E., Roman, I., 2001. Dynamic fracturing: field and experimental observations. *J. Struct. Geol.* 23 (8), 1223–1239.
- Savage, H.M., Brodsky, E.E., 2011. Collateral damage: evolution with displacement of fracture distribution and secondary fault strands in fault damage zones. *J. Geophys. Res. Solid Earth*. <https://doi.org/10.1029/2010JB007665>.
- Scholz, C.H., 2019. *The Mechanics of Earthquakes and Faulting*. Cambridge university press.
- Scibek, J., 2020. Multidisciplinary database of permeability of fault zones and surrounding protolith rocks at world-wide sites. *Sci. Data* 7 (1), 1–14.
- Shipton, Z.K., Cowie, P.A., 2003. A conceptual model for the origin of fault damage zone structures in high-porosity sandstone. *J. Struct. Geol.* [https://doi.org/10.1016/S0191-8141\(02\)00037-8](https://doi.org/10.1016/S0191-8141(02)00037-8).
- Schultz, R.A., Soliva, R., Fossen, H., Okubo, C.H., Reeves, D.M., 2008. Dependence of displacement-length scaling relations for fractures and deformation bands on the volumetric changes across them. *J. Struct. Geol.* 30 (11), 1405–1411.
- Smeraglia, L., Mercuri, M., Tavani, S., Pignalosa, A., Kettermann, M., Billi, A., Carminati, E., 2021. 3D Discrete Fracture Network (DFN) models of damage zone fluid corridors within a reservoir-scale normal fault in carbonates: multiscale approach using field data and UAV imagery. *Mar. Petrol. Geol.* 126, 104902.
- Snow, D.T., 1969. Anisotropic permeability of fractured media. *Water Resour. Res.* 5 (6), 1273–1289.
- Thiele, S.T., Grose, L., Samsu, A., Mickelthwaite, S., Vollgger, S.A., Cruden, A.R., 2017. Rapid, semi-automatic fracture and contact mapping for point clouds, images and geophysical data. *Solid Earth*. <https://doi.org/10.5194/se-8-1241-2017>.
- Tondi, E., Rustichelli, A., Cilona, A., Balsamo, F., Storti, F., Napoli, G., Agosta, F., Renda, P., Giorgioni, M., 2016. Hydraulic properties of fault zones in porous carbonates, examples from central and southern Italy. *Italian J. Geosci.* <https://doi.org/10.3301/IJG.2015.08>.

- Torabi, A., Ellingsen, T.S.S., Johannessen, M.U., Alaei, B., Rotevatn, A., Chiarella, D., 2020. Fault zone architecture and its scaling laws: where does the damage zone start and stop? *Geol. Soc. Lond. Special Publ.* 496 (1), 99–124.
- Trippetta, F., Carpenter, B.M., Mollo, S., Scuderi, M.M., Scarlato, P., Collettini, C., 2017. Physical and transport property variations within carbonate-bearing fault zones: insights from the Monte Maggio Fault (Central Italy). *G-cubed* 18 (11), 4027–4042.
- Vezzani, L., Ghisetti, F., 1998. *Carta Geologica dell'Abruzzo*. S.E.L.C.A., Firenze.
- Vezzani, L., Festa, A., Ghisetti, F.C., 2010. *Geology and Tectonic Evolution of the Central-Southern Apennines, Italy*, 469. Geological Society of America.
- Volatili, T., Zambrano, M., Ciloni, A., Huisman, B.A.H., Rustichelli, A., Giorgioni, M., Vittori, S., Tondi, E., 2019. From fracture analysis to flow simulations in fractured carbonates: the case study of the Roman Valley Quarry (Majella Mountain, Italy). *Mar. Petrol. Geol.* 100, 95–110. <https://doi.org/10.1016/j.marpetgeo.2018.10.040>. July 2018.
- Wilson, J.E., Chester, J.S., Chester, F.M., 2003. Microfracture analysis of fault growth and wear processes, Punchbowl Fault, San Andreas system, California. *J. Struct. Geol.* [https://doi.org/10.1016/S0191-8141\(03\)00036-1](https://doi.org/10.1016/S0191-8141(03)00036-1).
- Westphal, H., Eberli, G.P., Smith, L.B., Grammer, G.M., Kislak, J., 2004. Reservoir characterization of the Mississippian Madison formation, Wind river basin, Wyoming. *AAPG Bull.* 88 (4), 405–432.
- Wood, A.M., Paton, D.A., Collier, R.E.L.L., 2015. The Missing Complexity in Seismically Imaged Normal Faults: what Are the Implications for Geometry and Production Response? Geological Society Special Publication. <https://doi.org/10.1144/SP421.12>.
- Wrona, T., Fossen, H., Lecomte, I., Eide, C.H., Gawthorpe, R.L., 2020. Seismic expression of shear zones: insights from 2-D point-spread-function based convolution modelling. *J. Struct. Geol.* <https://doi.org/10.1016/j.jsg.2020.104121>.
- Zambrano, M., Tondi, E., Korneva, I., Panza, E., Agosta, F., Janiseck, J.M., Giorgioni, M., 2016. Fracture properties analysis and discrete fracture network modelling of faulted tight limestones, Murge Plateau, Italy. *Italian J. Geosci.* 135 (1), 55–67.
- Zambrano, M., Pitts, A.D., Salama, A., Volatili, T., Giorgioni, M., Tondi, E., 2019. Analysis of fracture roughness control on permeability using SfM and fluid flow simulations: implications for carbonate reservoir characterization. *Geofluids*. <https://doi.org/10.1155/2019/4132386>, 2019.